國立臺灣大學理學院化學系

碩士論文

Department of Chemistry

College of Science

National Taiwan University

Master Thesis

以紫外線吸收光譜法測量甲基乙烯基酮氧化物

（一種共振穩定的克里奇中間體）的反應動力學

Kinetics of Methyl Vinyl Ketone Oxide, A

Resonance-Stabilized Criegee Intermediate, Studied by

UV Absorption Spectrometry

林妍秀

Yen-Hsiu Lin

指導教授：林志民 博士

Advisor: Jim Jr-Min Lin, Ph.D.

中華民國 109 年 6 月

June 2020

摘要

　　由烯類的臭氧化反應產生的克里奇中間體是大氣中很活潑的氧化劑，會和二氧化硫、二氧化氮、水蒸氣、有機酸、無機酸等氣體分子反應，或單分子分解產生氫氧自由基，進而影響大氣的氧化能力及酸雨、氣膠等之形成。

　　異戊二烯是大氣中含量最豐富的烯類，臭氧化異戊二烯將產生最簡單的克里奇中間體(CH_2OO)、甲基乙烯基酮氧化物($CH_3(C_2H_3)COO$，簡稱 MVKO)及甲基丙烯醛氧化物($H_2C=C(CH_3)CHOO$)。MVKO 及 $H_2C=C(CH_3)CHOO$ 為共振穩定的克里奇中間體，目前直接觀測此種克里奇中間體的研究並不多，我們預期共振穩定結構將影響此種克里奇中間體的反應動力學行為。

　　我們實驗室使用 Barber *et al.* (*J. Am. Chem. Soc.,* **2018**, *140*, 10866)所發表的方法來產生 MVKO ($ICH_2CHCICH_3 + h\nu \rightarrow CH_3(C_2H_3)CI + I$，$CH_3(C_2H_3)CI + O_2 \rightarrow CH_3(C_2H_3)COO + I$)，並根據 Vansco *et al.* (*J. Chem. Phys.,* **2018**, *149*, 244309) 及 Caravan *et al.*(包括我們實驗室) (*Proc. Natl. Acad. Sci. U.S.A.*, **2020**, *117*, 9733-9740) 報導的 MVKO 紫外光吸收光譜，藉著測量 MVKO 對 340 nm 紫外光吸收度隨時間的變化，來觀察其反應動力學。我們發現在高壓(>100 Torr)下，MVKO 有個較慢的生成過程(約 1-2 ms)，我們推測此過程可能是加成物的分解反應($CH_3(C_2H_3)CIOO \rightarrow CH_3(C_2H_3)COO + I$)，據此提出的動力學模型可描述 MVKO 濃度隨時間的變化。實驗測得加成物分解反應具有正溫度效應，活化能為(14.0 ± 0.9) kcal mol^{-1}；此值與我們實驗室 (Lin *et al., Phys. Chem. Chem. Phys.*, **2020**, *22*, 13603) 報導的理論計算的加成物分解所需能量 14.0 kcal mol^{-1} 相近。加成物較 MVKO 穩定，但推測由於加成物不像 MVKO 具有共振穩定結構，加成物與 MVKO 的能量差僅有 14.0 kcal mol^{-1}，因此我們才能在微秒尺度觀測到加成物分解為 MVKO 的反應。

　　我們測量 MVKO 跟二氧化硫的反應，求得反應速率常數在 298 K 為(4.0 ± 0.6) x 10^{-11} cm^3 s^{-1}，且在 4-703 Torr 之間沒有明顯的壓力效應，活化能為(-3.1 ± 0.8)

kcal mol^{-1}，負的活化能代表此反應的過渡態能量低於反應物。我們也量測甲基乙

烯基酮氧化物的單分子分解反應，求得反應速率常數在 299 K 為(71±18) s^{-1}，且在

100-503 Torr 沒有明顯的壓力效應，活化能為(8.3±2.5) kcal mol^{-1}。跟小型克里奇中

間體比較，MVKO 在 299 K 的單分子反應速率常數比最簡單的克里奇中間體

(CH$_2$OO, (0.19±0.07) s^{-1} at 297±1 K)快，但比 *syn*-甲基取代克里奇中間體

(*syn*-CH$_3$CHOO, 122 s^{-1})跟雙甲基取代的克里奇中間體((CH$_3$)$_2$COO, 361 s^{-1})慢

(*Chem. Soc. Rev.*, **2017**, *46*, 7483-7497.)。依據實驗結果，我們推測 MVKO 在大氣中
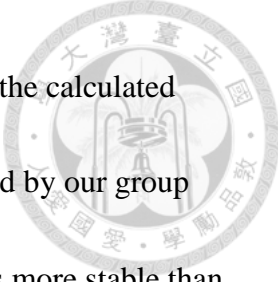
的主要分解途徑為單分子分解反應。

關鍵詞：克里奇中間體、紫外光吸收光譜、氣態反應動力學、雙分子反應、單分

子分解反應

Abstract

Criegee intermediates, known as carbonyl oxides, are very reactive species

generated from ozonolysis of alkenes. Criegee intermediates can react with atmospheric

gases, such as SO_2, NO_2, H_2O, organic acid, inorganic acid, volatile organic compounds

(VOCs), etc. and the unimolecular decomposition of Criegee intermediates generate OH

radicals. These processes play important roles in atmospheric chemistry.

Isoprene is the most abundant alkene in the atmosphere. Ozonolysis of isoprene

generates the simplest Criegee intermediate (CH_2OO), methyl vinyl ketone oxide

($CH_3(C_2H_3)COO$, MVKO), and methacrolein oxide ($H_2C=C(CH_3)CHOO$, MACRO).

Our group used the method reported by Barber *et al.* (*J. Am. Chem. Soc.,* **2018**, *140*,

10866) to generate MVKO ($ICH_2CHCICH_3 + h\nu \rightarrow CH_3(C_2H_3)CI + I$，$CH_3(C_2H_3)CI +$

$O_2 \rightarrow CH_3(C_2H_3)COO + I$). Utilizing the UV absorption spectrum reported by Vansco *et*

al. (*J. Chem. Phys.,***2018**, *149*, 244309) and Caravan *et al.*(including our group) (*Proc.*

Natl. Acad. Sci. U.S.A. **2020**, *117*, 9733-9740), we studied the kinetics of MVKO with

its UV absorption at 340 nm. We found that at high pressure (>100 Torr), there ia a slow

process of MVKO formation (1-2 ms). We assume that this slow formation of MVKO is

from the decomposition of the adduct ($CH_3(C_2H_3)CIOO \rightarrow CH_3(C_2H_3)COO + I$). Based

on this adduct mechanism, our kinetic model agrees very well with the experimental

observations of MVKO kinetics. The activation energy of the decomposition of the

adduct was measured to be (14.0±0.9) kcal mol^{-1}, which is similar to the calculated

energy difference between $CH_3(C_2H_3)CIOO$ and (MVKO + I) reported by our group

(Lin *et al., Phys. Chem. Chem. Phys.*, **2020**, *22*, 13603). The adduct is more stable than

MVKO. However, because the adduct has no resonance-stabilized structure like MVKO,

the energy difference between the adduct and MVKO is only 14.0 kcal mol^{-1}, and the

rate coefficient of the formation of MVKO from the adduct can reach ~10^3 s^{-1} at room

temperature.

We studied the kinetics of the reaction of MVKO with SO_2; the observed reaction

rate coefficient is (4.0±0.6) x 10^{-11} cm^3 s^{-1} at 298 K with an insignificant pressure effect

in range 4-703 Torr. The activation energy was measured to be (−3.1±0.8) kcal mol^{-1}. A

negative activation energy means that the transition state energy is lower than that of the

reactants. We also studied the unimolecular decomposition of MVKO, and the rate

coefficient was determined to be (71±18) s^{-1} at 299 K with an insignificant pressure

effect for 100-503 Torr. The measured activation energy is (8.3±2.5) kcal mol^{-1} at 302

Torr and 278-319 K. Comparing with small Criegee intermediates, the measured

unimolecular decomposition rate coefficient of MVKO at 299 K is larger than that of

CH_2OO ((0.19±0.07) s^{-1} at 297±1 K), and smaller than those of *syn*-CH_3CHOO (122 s^{-1})

and $(CH_3)_2COO$ (361 s^{-1}). According to the experimental results, we conclude that the

dominant removal pathway for MVKO in the atmosphere is its unimolecular

iv

decomposition.

Table of Contents

List of Tables

Chapter 1. Introduction

Criegee intermediates, also known as carbonyl oxides, are generated through

ozonolysis of alkene in the atmosphere.[1] Criegee intermediates can react with

atmospheric gases, such as SO_2, NOx, H_2O, organic acid, inorganic acid, volatile

organic compounds (VOCs), etc. Also, the unimolecular decomposition of Criegee

intermediates generates OH radicals, which plays an important role in atmospheric

chemistry.[2]

Before 2012, the direct measurement of the Criegee intermediate in kinetic studies

was unachievable. The steady-state concentration of the Criegee intermediate is

estimated by Equation 1 below.

$$[CI]_{s.s.} = \frac{k_{alkene+O_3}[alkene][O_3]}{k_{uni} + k_{CI+O_3}[O_3] + k_{CI+alkene}[alkene] + k_{CI+product}[product]} \quad \text{(Equation 1)}$$

where $k_{alkene+O3}$ represents the reaction rate coefficient of ozone with alkene, which is

only $\sim10^{-17}$ cm^3 s^{-1};[3] k_{uni} indicated the unimolecular decay rate of Criegee intermediates,

which is $\sim10^1$-10^3 s^{-1} dependent on the structure of Criegee intermediates;[4-6] k_{CI+O3} is

the reaction rate coefficient of Criegee intermediates with ozone, which has been

reported to be 6.7 x 10^{-14} cm^3 s^{-1} for CH_2OO;[7] $k_{CI+alkene}$ means the reaction rate

coefficient of Criegee intermediates with alkene, which has been reported to be 1.5 x

10^{-15} cm^3 s^{-1} for the reaction of CH_2OO with isoprene;[8] $k_{CI+product}$ is the reaction rate

1

coefficient of Criegee intermediate with products, such as aldehyde, ketone, acid, etc,

the reaction rate coefficients of Criegee intermediates with acids has been reported to be

$\sim 10^{-10}$-10^{-11} cm^3 s^{-1}.[6, 9]

Assume [alkene] = 10^{10} cm^{-3}, [O$_3$] = 10^{12} cm^{-3}, and the reaction rate coefficients of

Criegee intermediates + O$_3$ and Criegee intermediates + alkene can be represented by

the rate coefficients of CH$_2$OO + O$_3$ and CH$_2$OO + isoprene, the steady-state

concentration of Criegee intermediates is estimated to be:

$$[CI]_{s.s.} = \frac{10^{-17}\left(cm^3\ s^{-1}\right)\cdot 10^{10}\left(cm^{-3}\right)\cdot 10^{12}\left(cm^{-3}\right)}{\left(10^1\text{-}10^3\right)\left(s^{-1}\right)+6.7\times10^{-14}\left(cm^3\ s^{-1}\right)\cdot 10^{12}\left(cm^{-3}\right)+1.5\times10^{-15}\left(cm^3\ s^{-1}\right)\cdot 10^{10}\left(cm^{-3}\right)+k_{CI+product}[product]}$$
$$\sim 10^2\text{-}10^4\left(cm^{-3}\right)$$

which is too low to be measured directly.

If we increase the concentration of alkene and O$_3$ to obtain higher concentration of

Criegee intermediates, the concentration of byproducts, such as aldehyde, ketone, and

acid, would also increase. The reaction of Criegee intermediates with byproducts would

make the kinetics of Criegee intermediates too complicated to be solved.

The reaction rate coefficients obtained from indirect measurements have a large

scatter of several orders of magnitude.[5, 10] At 2012, Taatjes *et al.* reported a method to

generate the simplest Criegee intermediate (CH$_2$OO) through the reaction of O$_2$ and a

iodo-alkyl radical, produced from the photolysis of diiodomethane (CH$_2$I$_2$ + $h\nu \rightarrow$ CH$_2$I

2

+ I; $CH_2I + O_2 \rightarrow CH_2OO + I$), and directly measured the kinetics of Criegee

intermediate for the first time.[11] Many researches on small alkyl Criegee intermediates

(CH_2OO, CH_3CHOO, $(CH_3)_2COO$, CH_3CH_2CHOO) emerged since then, and there have

been several reviews to summary these works.[6, 12-18] However, due to the lack of proper

precursors, the researches on large and non-alkyl Criegee intermediates are relatively

scarce.

Isoprene is the most abundant alkene in the atmosphere.[19] The ozonolysis of

isoprene can generate three kinds of Criegee intermediates, which are methyl vinyl

ketone oxide ($CH_3(C_2H_3)COO$, MVKO, yield = 0.23), formaldehyde oxide (CH_2OO,

yield = 0.58), and methacrolein oxide (CH_3CCH_2CHOO, MACRO, yield = 0.19).[4]

Both MVKO and MACRO are resonance-stabilized vinyl substituted Criegee

intermediates. However, it is difficult to study their individual kinetics from the

ozonolysis of isoprene.[20, 21]

At 2018, Barber *et al.* reported a new method to produce methyl vinyl ketone oxide

from the reaction of O_2 and an iodo-alkenyl radical, which was produced from the

photolysis of 1,3-diiodo-2-butene ($ICH_3CHCICH_3 + h\nu \rightarrow CH_3(C_2H_3)CI + I$;

$CH_3(C_2H_3)CI + O_2 \rightarrow CH_3(C_2H_3)COO$ (MVKO) + I).[4] This method made the direct

measurement of MVKO in kinetic studies possible. There are four possible conformers

of MVKO, which are *syn-trans*-MVKO, *syn-cis*-MVKO, *anti-trans*-MVKO, and

3

anti-cis-MVKO; *syn* and *anti* refer to the orientation of methyl group with respect to the

terminal oxygen, while *trans* and *cis* refer to the orientation of the C=C and C=O double

bond. The calculated barrier for the *trans-cis* isomerization is lower than that of the

s*yn-anti* isomerization. *syn-trans*-MVKO is the most stable conformer.[4] (See Figure 1)
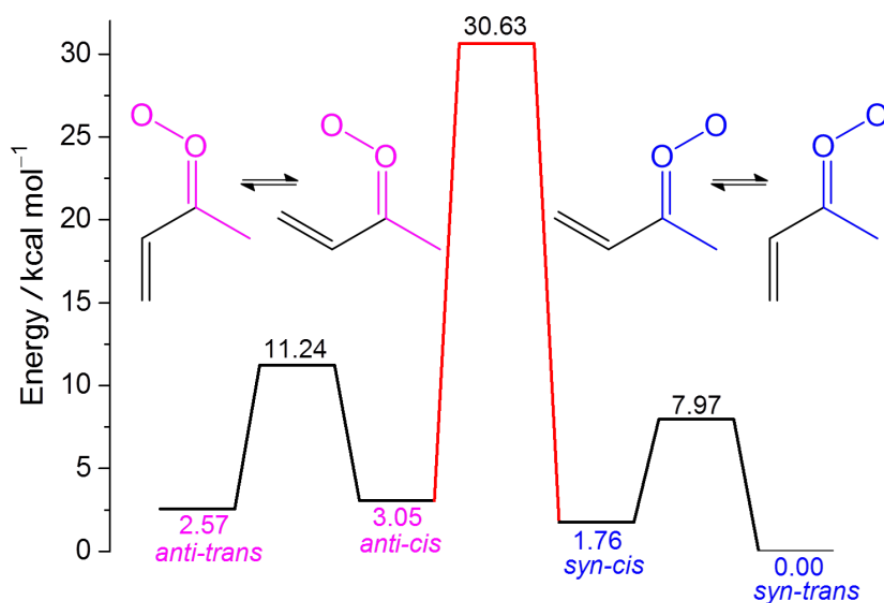
Figure 1. Four conformers of MVKO with their calculated zero-point-corrected energies.

The calculated isomerization barriers are also shown. The calculated values are adapted

from Barber *et al*.[4] Geometries optimization is done at the B2PLYP-D3/cc-pVTZ level,

and energies are calculated at the ANL0-B2F level. The stationary point energy for the

transition state of *anti-cis*-MVKO to *syn-cis*-MVKO is calculated by

CCSD(T)-F12b/cc-pVTZ-F12 with some corrections.

4

Barber *et al.* used an infrared laser to pump MVKO and probed the OH radical

product with laser induced fluorescence. IR spectrum of MVKO was measured with this

IR pump-UV probe system. All four conformers of MVKO were observed. The

energy-dependent unimolecular decay rate coefficients $k(E)$ of MVKO were also

obtained through the formation rate coefficient of OH radicals from MVKO excited in

the region of CH stretch overtone (2νCH). The thermal-dependent unimolecular decay

rate coefficient $k(T)$ was predicted through the extension of $k(E)$ with the master

equation modeling. For *syn*-MVKO, the thermal rate coefficient for unimolecular decay

was calculated to be 33 s^{-1} at 298K, and that for *anti*-MVKO was reported to be 2140

s^{-1}.[4]

Vansco *et al.* used the same method as Barber *et al.* to generate MVKO in pulsed

supersonic expansion. MVKO was excited at its first $\pi^* \leftarrow \pi$ electronic band with

tunable UV-Vis light at 305-480 nm before being ionized with vacuum ultraviolent

photoionization at 118 nm. The UV spectrum of MVKO with peak at 388 nm was

measured from the depletion of the mass signal at m/z = 86 channel (MVKO, m = 86).[22]

At 2020, Caravan *et al*. (including our group) reported the UV absorption spectrum of

MVKO at 298 K with multi-pass broadband probe light. The peak of the spectrum was

at 370.6 nm with full width at half maximum (FWHM) of 73.4 nm.[9] Comparing the UV

spectrum of MVKO with that of small alkyl Criegee intermediates,[23-26] we could find

5

that the spectrum of MVKO was red-shifted. This result is consistent with the previous

theoretical research.[27]

Our group generated MVKO with the method reported by Barber *et al*

$(ICH_3CHCICH_3 + h\nu \rightarrow CH_3(C_2H_3)CI + I; CH_3(C_2H_3)CI + O_2 \rightarrow CH_3(C_2H_3)COO$
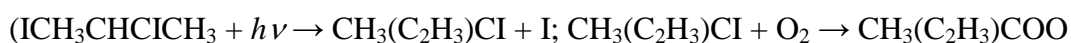
$(MVKO) + I)$[4] and studied the kinetics of MVKO via its strong UV absorption. The

detail of experimental setup is in chapter 2. We measured the reaction rate coefficient of

MVKO with SO_2 at 4-703 Torr. Also, we observed that the behavior of MVKO

generation depends on pressure and used a model with the formation of MVKO from an

adduct to explain this phenomenon. The recorded time traces of MVKO were fitted well

with the model considering the adduct kinetics. The results and discussion about the

kinetics of the adduct as well as the reaction of MVKO with SO_2 are in chapter 3.

Chapter 4 discusses the unimolecular decomposition of MVKO. The unimolecular

reaction of MVKO was measured in 100-503 Torr and at 278-319 K.

Chapter 2. Experimental setup

2.1 Production of MVKO

We followed the innovative method of Barber *et al.* to produce MVKO. The related

reactions were listed below (R1-R2). MVKO was generated from the reaction of O_2

with the radical produced from laser photolysis of (Z)-1,3-diiodo-2-butene (Accela, >

98.1 % by gas chromatography).[4]

$$ICH_2CHCICH_3 + h\nu \rightarrow CH_3(C_2H_3)CI + I \qquad (R1)$$

$$CH_3(C_2H_3)CI + O_2 \rightarrow CH_3(C_2H_3)COO \ (MVKO) + I \qquad (R2)$$
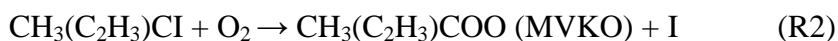
The 248-nm KrF excimer laser (Coherent, CompExPro 205F) was used for the

photolysis light source. The precursor (1,3-diiodo-2-butene)/O_2/N_2 flow was mixed with

the reactant SO_2/N_2 flow right before entering the reactor. The reaction gases were

injected through the middle of the reactor and were pumped out from two ends. All gas

flows were controlled by mass flow controllers (Brooks, 5850E/Bronkhost FG-201 CV).

The gases in the reactor were adjusted to fully refresh between each laser pulse.

(Photolysis rate: 0.55-1.7 Hz)

2.2 Light path

The UV spectrum of MVKO has been reported by Vansco *et al.* (peak at 388 nm)[22] and Caravan *et al.* (peak at 370.6 nm with FWHM of 73.4 nm; see Figure 3)[9]. We measured MVKO with its strong UV absorption at 340 nm to avoid the signal of byproduct IO. A broadband Xe lamp (Energetiq, EQ-99) was used as the probe light source and was focused by an achromatic lens (f = 100 mm, Thorlabs, ACA254-100-UV) to the reactor. The reactor was glass tube with inner diameter 1.9 cm and length 80 cm, sealed with anti-reflection SiO_2 windows (Edmund, 65875) at two ends. To prevent windows from contamination, N_2 flowed from two sides for purges and reduced the effective sample length to 71 cm. To enhance the absorption signal, the probe light was reflected six times through the reactor by a prism (Thorlabs, PS609, fused silica, right-angle, uncoated, 5 mm) and a spherical mirror (R=1m, Thorlabs, CM750-500-F01). The effective light path was therefore 426 cm. The signal was then reflected by another prism and mirrors (Edmund, 68315 or 48016), and was focused by a lens (f = 50 mm) to the balanced photodiode detector (Thorlabs, PDB450A). The reference beam was focused by another achromatic lens (f = 150 mm, Thorlabs, ACA254-150-UV), and passed through a neutral density filter for tuning the intensity to be similar to that of the signal beam. The reference beam was reflected by mirrors (Edmund, 68315 or 48016) and was focused to the balanced photodiode detector

8

(Thorlabs, PDB450A). Both signal and reference beam went through a 340 nm

bandpass filter (Edmund Optics, 65129, 10 nm OD4) in front of the detector to select

the probe wavelength. Figure 2. shows the schematic diagram of our optical light path.

The signals were recorded with the oscilloscope (LeCroy, HDO4034). The time traces

of 60-120 laser pulses were averaged to improve the signal-to-noise ratio.
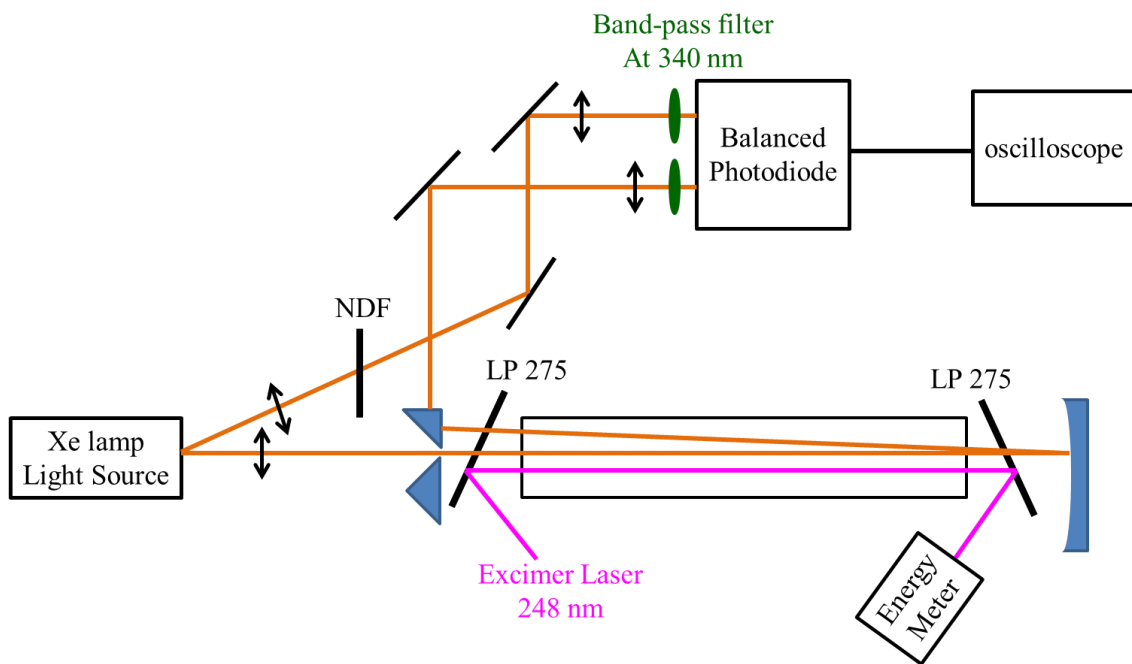
Figure 2. Schematic diagram of the optical light path. NDF: neutral density filter. LP

275: long-pass filter at 275 nm. This figure is adapted from Chao et al.[28]
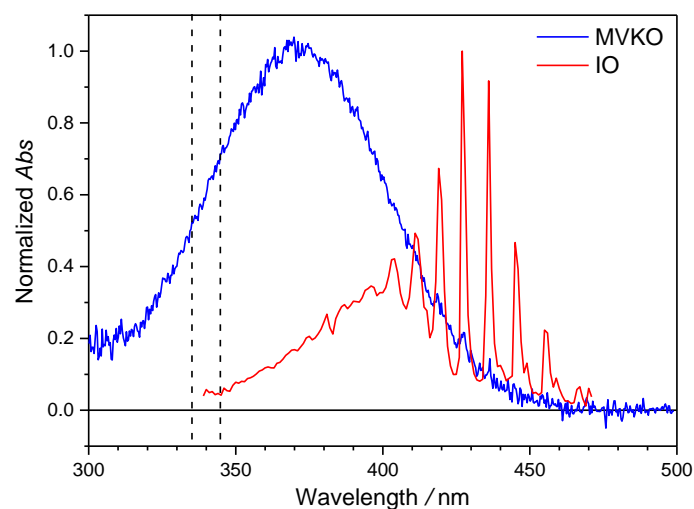
Figure 3. Blue line: UV absorption spectrum of MVKO at 298 K recorded in our

laboratory; it has been reported by Caravan *et al*.[9] Red line: UV absorption spectrum of

byproduct IO.[29] The range between the two dashed lines represents our probe

wavelength range (340±5) nm.

The 248 nm photolysis laser beam passed through an attenuator and was focused by

a cylindrical lens (1m). Two long pass filters (Asahi Spectra Co., Ltd. UV 275 nm, 25

mm dia. F0201 & F0204) were placed in the two ends of the reactor, and coupled the

photolysis laser pulse in and out of the reactor. After reflected out of the reactor, the

laser pulse energy was measured by an energy meter (Gentec EO, UP25N-100H-H9-D0

for the experiments of the reaction of MVKO with SO_2) or a thermal meter (Gentec EO,

QE25SP-H-MB-D0 for the experiments of the unimolecular decomposition of MVKO).

10

The laser pulse was triggered by a delay generator (DG535), and the data recording was

controlled by a LabView program.

2.3 The measurements of the concentrations of SO$_2$ and 1,3-diiodo-2-butene

Both the concentrations of 1,3-diiodo-2-butene and SO$_2$ were determined by UV

absorption spectrum. The measurements for 1,3-diiodo-2-butene and SO$_2$ were

performed in two glass cells separately (length = 90 or 75.3 cm for 1,3-diiodo-2-butene

/ 90 cm for SO$_2$; diameter = 1.2 cm for both cases). Deuterium lamps (Hamamatsu,

L10904) were used as the probe light sources and the detectors were mini spectrometers

(Ibsen FHW-380 for SO$_2$ and Ocean Optics, FLAME-S-XR1-ES for

1,3-diiodo-2-butene).

SO$_2$ (Matheson, 99.98 %) was diluted in a ~2 L stainless steel cylinder with N$_2$

before the experiments. To get the concentration of SO$_2$, we used Beer's law with

Equation 2.

$$[\text{SO}_2]_{\text{cell}} = \frac{\int_{\lambda=200\text{nm}}^{\lambda=250\text{nm}} Abs_{\text{SO}_2\_\text{cell}}(\lambda)d\lambda}{L_{\text{SO}_2\_\text{cell}} \cdot \int_{\lambda=200\text{nm}}^{\lambda=250\text{nm}} \sigma_{\text{SO}_2}(\lambda)d\lambda} \text{ or } \frac{\int_{\lambda=200\text{nm}}^{\lambda=350\text{nm}} Abs_{\text{SO}_2\_\text{cell}}(\lambda)d\lambda}{L_{\text{SO}_2\_\text{cell}} \cdot \int_{\lambda=200\text{nm}}^{\lambda=350\text{nm}} \sigma_{\text{SO}_2}(\lambda)d\lambda}$$

(Equation 2)

where [SO$_2$]$_{\text{cell}}$ is [SO$_2$] in the glass cell, $L_{\text{SO2\_cell}}$ is the light path length in the glass cell,

which is 90 cm, $Abs_{\text{SO2\_cell}}(\lambda)$ represents the absorbance of SO$_2$ in the glass cell, σ_{SO2}

11
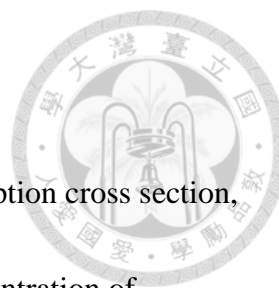
indicates the cross section of SO_2.[30]

As for 1,3-diiodo-2-butene, due to the lack of absolute UV absorption cross section, the concentration could not be derived. Thus, we presented the concentration of precursor by its absorbance (Abs_{prec}) at 238.5 nm in the reactor.

$[SO_2]$ and Abs_{prec} in the photolysis reactor were derived by considering flow mixing ratio, temperature, and pressure difference between the cell and the reactor by assuming ideal gas behavior as Equations 3-5. (For Abs_{prec}, the difference between effective light paths of the cell and the reactor was also considered.) The temperature and pressure of the cell were measured by a temperature meter (Rotronics, HC2-S) tied on the cell and gauges (INFICON, CDG025D 1000 Torr) connected in the middle.
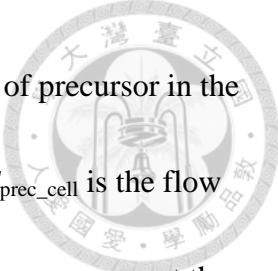
$$[SO_2]_{reactor} = [SO_2]_{cell} \frac{F_{SO_2\_cell}}{F_{reactor}} \frac{P_{reactor}}{P_{SO_2\_cell}} \frac{Temp_{SO_2\_cell}}{Temp_{reactor}} \quad \text{(Equation 3)}$$

where F_{SO2_cell} is the flow through the glass cell for $[SO_2]$ measurement, $F_{reactor}$ is the total flow through the reactor, P_{SO2_cell} and $Temp_{SO2\_cell}$ represent the pressure and temperature of the glass cell for $[SO_2]$ measurement. $P_{reactor}$ and $Temp_{reactor}$ indicate the pressure and temperature of the reactor.

$$-\ln T_{prec} = Abs_{prec\_cell} \quad \text{(Equation 4)}$$

$$Abs_{prec\_reactor} = Abs_{prec\_cell} \frac{F_{prec\_cell}}{F_{reactor}} \frac{P_{reactor}}{P_{prec\_cell}} \frac{Temp_{prec\_cell}}{Temp_{reactor}} \frac{L_{reactor}}{L_{prec\_cell}}$$

(Equation 5)

12

where T_{prec} and Abs_{prec_cell} represent the transmittance and absorbance of precursor in the glass cell, $Abs_{prec\_reactor}$ is the absorbance of precursor in the reactor, F_{prec_cell} is the flow through the glass cell for precursor measurement, P_{prec_cell} and $Temp_{prec\_cell}$ represent the pressure and temperature of the glass cell for precursor measurement. $L_{reactor}$ is the length of effective optical path in the reactor, which is 426 cm. L_{prec_cell} is the length of light path in the glass cell, which is 75.3 or 90 cm.

2.4 Impurity in 1,3-diiodo-2-butene (sample)

We used a quadruple mass spectrometer (Stanford Research Systems, RGA 200) to check the impurity in the precursor sample during the experiments. The schematic setup of RGA is shown in Figure 4. The precursor was carried out by a He flow, and a small amount of precursor / He flow was sent to RGA through a jet separator made of capillary tubes. The RGA system was pumped by a turbo pump (PFEIFFER, TMU 064) to around 10^{-6}-10^{-7} Torr, and the pressure was measured by an ion gauge (Granville-Phillips). A mechanical pump (Edwards, RV Two Stage 12) served as the backing pump for the turbo pump, and was also used to pump the jet separator to ~10^{-2} Torr while the pressure in the reactor was ~10^2 Torr. The result of the RGA was shown in Figure 5. We started the mass spectrum scan from m/z = 47 to avoid saturating the detector by the large signal of carbon dioxide (m/z = 44). The nominal mass of the

13
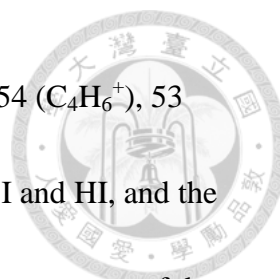
precursor ($C_4H_6I_2$) is 308 amu, and possible daughter ions are m/z = 54 ($C_4H_6^+$), 53

($C_4H_5^+$). The mass channels m/z = 127,128 represent the signal from I and HI, and the

signals of m/z = 55-126 could be from impurities. We checked the mass spectra of the

reactants in the synthesis process of the precursor,[4] but none of them match the

spectrum we measured. The possible sources of the impurities are unknown in this point.

Meanwhile, the mainstream of the precursor / He flow was mixed with an O_2 flow and a

buffer N_2 flow before flowing into the reactor and photolyzed by 248 nm laser pulses to

generate MVKO. (Photolysis rate: 3.01 Hz) The time traces were averaged for 100 laser

pulses, and shown in Figure 6. Equation 6 was used to fit the time traces. (k_{obs} indicates

the observed decay rate coefficient of the trace. More detail of the fitting model is

discussed in Chapter 3.2)

$$
\Delta Abs = \sigma L[\text{MVKO}](t) + C_0
$$

$$
= \sigma L \left\{ [\text{MKVO}]_{\text{total}} \{ \alpha\, e^{-k_{obs}t} + (1-\alpha)\frac{k_r}{k_r - k_{obs}}[e^{-k_{obs}t} - e^{-k_r t}]\} \right\} + C_0 \qquad \text{(Equation 6)}
$$

The temporal behaviors of specific m/z mass channels were recorded while the

time trace of MVKO was recorded. The results are shown in Figure 7. The observed

decay rate coefficient of MVKO (k_{obs}) did not correlate to the intensities of the impurity

mass peaks. Thus, even though there were some impurities in the precursor, these

impurities did not affect the kinetics of MVKO.

14
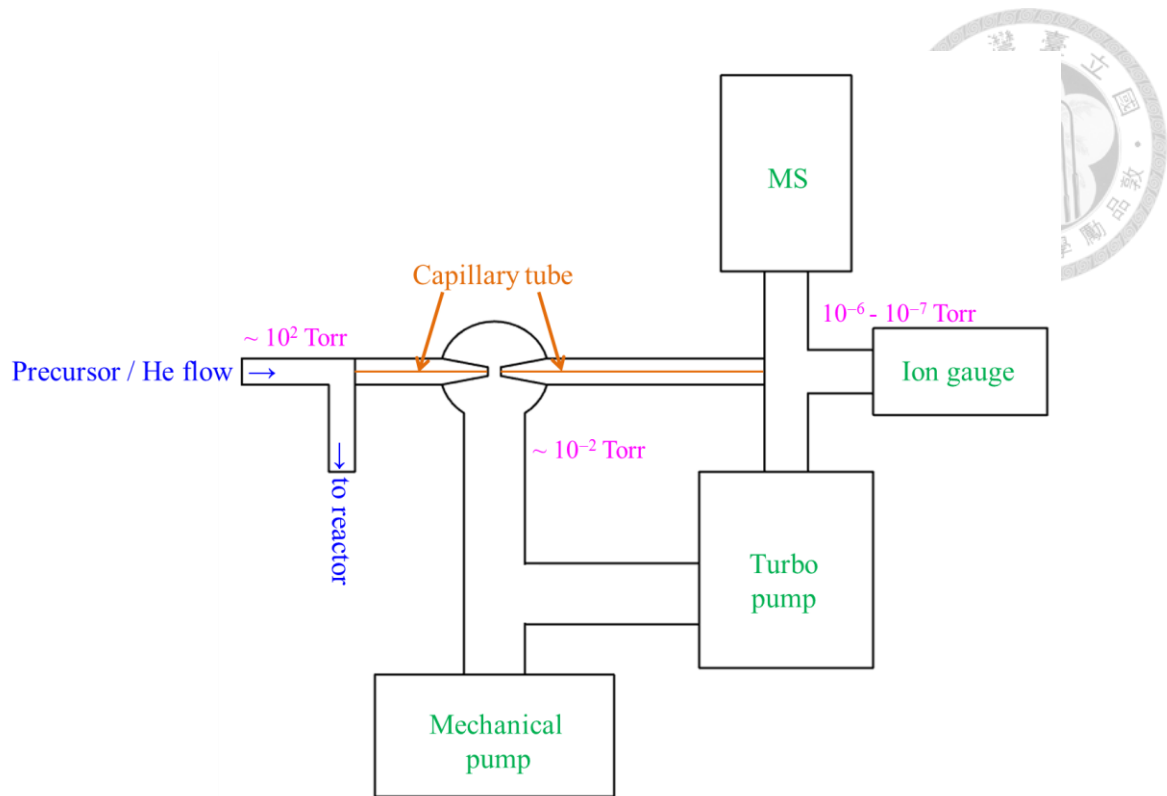
Figure 4. The experimental setup for the mass system (not to scale). The main stream of

the precursor / He flow is introduced to the reactor while a minor flow is sent to a

quadrupole mass spectrometer through a jet separator to measure the mass spectrum.
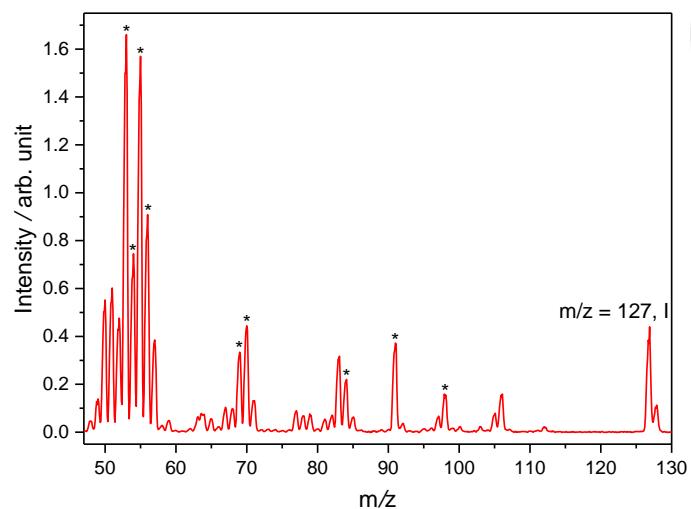
Figure 5. The mass spectrum of the precursor (1,3-diiodo-2-butene, $C_4H_6I_2$, m=308)

sample measured by RGA. The signal at m/z = 54 could be from $C_4H_6^+$, which could be

a daughter ion of the precursor. The peaks at m/z = 127, 128 mass channels represent

the signal of I and HI, and the peaks at m/z = 55-126 might be from impurities. The time

behaviors of the peaks with star marks (m/z = 53, 54, 55, 56, 69, 70, 84, 91, and 98

mass channel.) are recorded. (Figure 7. Upper panel)
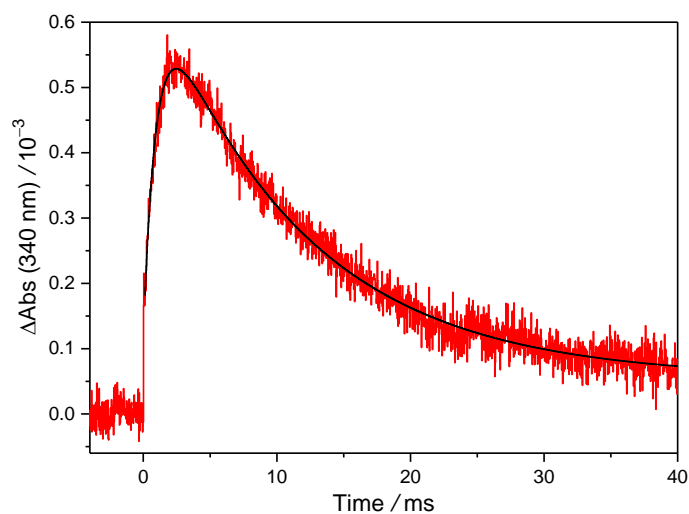
Figure 6. The observed time trace of MVKO while the precursor sample mass spectrum

is also recorded. (P = 300 Torr. P_{O2} = 11.2 Torr. T = 299 K. Laser fluence = 2.04 mJ

cm^{-2}. Abs_{prec} in the reactor = 0.03.) The time zero is set as the laser pulse. The probe

wavelength is (340±5) nm. The black curve represents the fitting result from Equation

6.
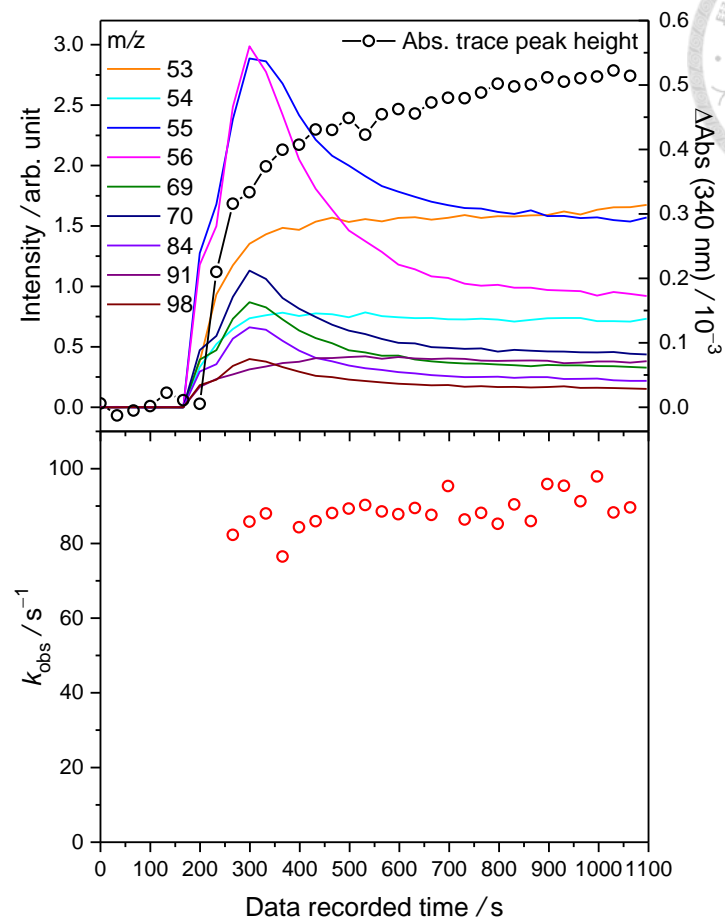
Figure 7. Upper panel: Representative time-dependent signals of m/z = 53, 54, 55, 56,

69, 70, 84, 91, 98 mass channels of the sample from RGA (left y-axis) & the time

profile of the maximum of the absorbance change of MVKO (right y-axis). Lower panel:

the time behavior of the observed decay rate coefficient (k_{obs}) of MVKO. The observed

decay rate coefficient does not correlate to the time behavior of most of the mass peaks,

for example, signals m/z = 55, 56 have pronounced peaks at ~300 s but the observed

decay rate coefficient does not correlate to them. The observed rate coefficient seems to

be quite consistent with time. (k_{obs} = (88.6 ± 4.53) s^{-1}, avg ± 1 std).

18

2.5 The temperature of the reactor

The reactor was a double-layer glass tube. The outer jacket was filled with water

circulated from a constant temperature bath (Yih Der BL-730) to control the

temperature of the reactor. The circulated water entered the outer jacket of the reactor

from two sides and went out from the middle. The water then flowed into a water bath

used to preheat and precool the mainstream of reaction gases through a ~ 75 cm long

copper tube before it circulated back to the constant temperature bath. To calibrate the

temperature of reaction gases, a resistance temperature detector (RTD) was stuck into

the reactor with N_2 flowing before the experiments. The temperature difference between

the gas temperature in the inner jacket and the water temperature in the outer jacket of

the reactor was less than 0.5 $^{\circ}$C. During experiments, 3 RTDs were placed at the two

ends and the middle of the reactor to measure the temperature of water at the outer

jacket of the reactor.

Chapter 3. Reaction of MVKO with SO₂ and Kinetics of the Adduct (CH₃(C₂H₃)CIOO)
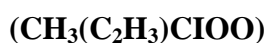
3.1 Time traces of MVKO at different pressure

The time traces of MVKO absorption signal under various [SO₂] at 4.2 Torr and 298 K are shown in Figure 8. The change of the absorbance after the photolysis laser pulse is proportional to the concentration of MVKO. From Figure 8, we can find that MVKO reacts with SO₂, and the time trace of MVKO decays faster under higher [SO₂].
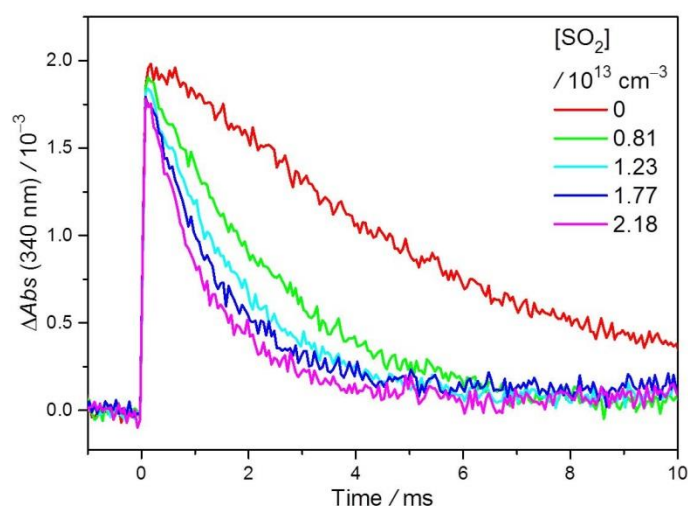
Figure 8. Typical time traces of absorbance change of MVKO at various [SO₂] at 4.2 Torr and 298 K. The data are from Table 1, Exp K1. The probe wavelength = (340±5) nm. The time zero is set as the photolysis laser pulse. At higher [SO₂], the signal of MVKO decays faster.

20

We also checked the time traces of MVKO at various [SO_2] at 102 Torr and 299 K. (See Figure 9) Unlike the time traces at 4.2 Torr, the prompt generation of MVKO right after the laser pulse is followed by a slow formation of MVKO at 102 Torr. The concentration of MVKO reaches its peak at around 1-2 ms delay time. The prompt generation is from the reaction of O_2 with the iodo-alkenyl radical. The rate coefficient has been reported to be 1.7 x 10^{-13} cm^3 s^{-1}.[9] At [O_2] ~ 10^{17} cm^{-3} in our experiments, the lifetime of the iodo-alkenyl radical would be <50 μs. To explain the slow formation of MVKO, we propose that in addition to MVKO (R2a), an adduct ($CH_3(C_2H_3)CIOO$) (R2b) is also generated in the reaction of O_2 with iodo-alkenyl radical ($CH_3(C_2H_3)CI$). The slow formation of MVKO is from the reaction of the adduct (R2c) with the observed lifetime of the adduct to be ~ms. At higher pressure, the adduct is easier to be stabilized; therefore, the yield of the adduct is higher.

$$ICH_2CHCICH_3 + h\nu \rightarrow CH_3(C_2H_3)CI + I \qquad\qquad (R1)$$

$$CH_3(C_2H_3)CI + O_2 \rightarrow CH_3(C_2H_3)COO + I \qquad\qquad (R2a,\ \alpha k_2)$$

$$CH_3(C_2H_3)CI + O_2 + M \rightarrow CH_3(C_2H_3)CIOO + M \qquad (R2b,\ (1-\alpha)k_2)$$

$$CH_3(C_2H_3)CIOO + M \rightarrow CH_3(C_2H_3)COO + I + M \qquad (R2c,\ k_r)$$

$$CH_3(C_2H_3)COO + SO_2 \rightarrow Products \qquad\qquad (R3,\ k_{SO2})$$

$$CH_3(C_2H_3)COO + X \rightarrow Products \qquad\qquad (R4,\ k_X)$$

21
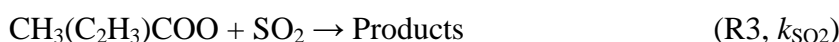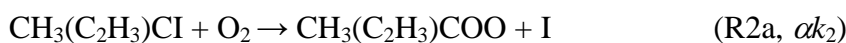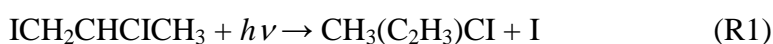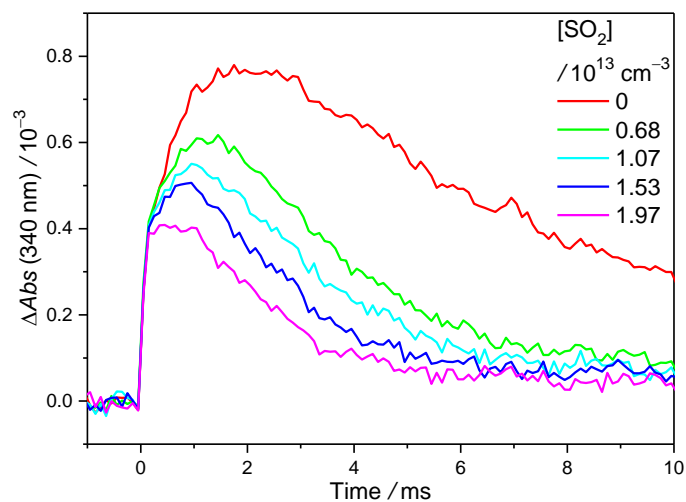
Figure 9. Time traces of the absorbance change of MVKO under various [SO$_2$] at 102

Torr and 299 K. The data are from Table 1, Exp K6a. The probe wavelength = (340±5)

nm. The time zero is set as the photolysis laser pulse.

To examine this idea, we did experiments at 31-702 Torr with the concentration of

the precursor and the laser fluence controlled to be constant. The result is shown in

Figure 10, and the yield of the adduct changes with pressure. The maximums of the

absorption signals are similar at 31-702 Torr, which means that all the adduct turns into

MVKO eventually.
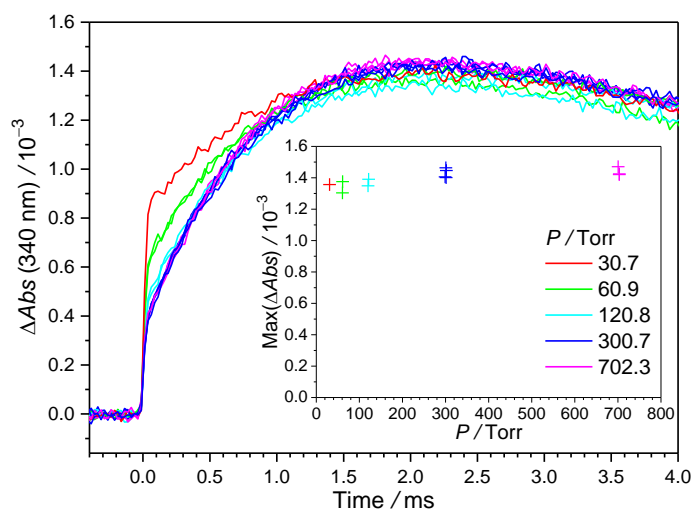
Figure 10. Time traces of MVKO at 31-702 Torr and 299 K with the concentration of the precursor and the laser fluence controlled to be constant. The probe wavelength is (340±5) nm. The time zero is when the photolysis laser pulse fired. P_{O2} = 11 Torr, N_2 balanced; T = 299 K; Abs_{prec} = 0.139; Laser fluence = 1.06 mJ cm^{-2}. Inset: plot of Max(ΔAbs) against pressure. Max(ΔAbs) is the average of ΔAbs during 1.8-2.4 ms normalized by the deviation of the concentration of precursor and the laser fluence (~ 2%).

23

3.2 Analysis

From processes R1-R4, we can write the equations below:

$$[CH_3(C_2H_3)CI](t) = [CH_3(C_2H_3)CI]_0 \exp(-k_2[O_2]t) \qquad \text{(Equation 7)}$$

$$[adduct](t) = \frac{(1-\alpha)k_2[O_2][CH_3(C_2H_3)CI]_0}{k_2[O_2] - k_r}[\exp(-k_r t) - \exp(-k_2[O_2]t)]$$

(Equation 8)

$$[MVKO] = \frac{k_2[O_2](1-\alpha)[CH_3(C_2H_3)CI]_0}{k_2[O_2] - k_r} \frac{k_r}{k_{obs} - k_r}[\exp(-k_r t) - \exp(-k_{obs}t)]$$

$$+ \left\{\frac{k_2[O_2](1-\alpha)[CH_3(C_2H_3)CI]_0}{k_2[O_2] - k_r} \frac{k_r}{k_{obs} - k_2[O_2]}\right\}[\exp(-k_{obs}t) - \exp(-k_2[O_2]t)]$$

$$- \frac{\alpha k_2[O_2][CH_3(C_2H_3)CI]_0}{k_{obs} - k_2[O_2]}[\exp(-k_{obs}t) - \exp(-k_2[O_2]t)]$$

(Equation 9)

where k_2 is the reaction rate coefficient of the iodo-alkenyl radical with O_2, and has been

reported to be 1.7 x 10^{-13} cm^3 s^{-1}.[9] α represents the yield of prompt MVKO from the

reaction of O_2 with iodo-alkenyl radical, $(1-\alpha)$ is the yield of the adduct from the

reaction of O_2 with iodo-alkenyl radical, k_r indicates the reaction rate coefficient of the

adduct $\rightarrow$ MVKO + I, k_{obs} means the observed decay rate coefficient of MVKO.

From mechanisms R1-R2 and Figure 10, we assume that the iodo-alkenyl radical

reacted with O_2 would all turn into MVKO or the adduct, and the adduct would all turn

into MVKO eventually. Thus, $[CH_3(C_2H_3)CI]_0$ can be written as $[MVKO]_{total}$. At $[O_2] \sim$

10^{17} cm^{-3} in our experiments, the lifetime of the iodo-alkenyl radical would be <50 μs.

Because the rate coefficient $k_2[O_2]$ (> 2 x 10^4 s^{-1}) is much larger than that of k_r or k_{obs}

(~10^2-10^3 s^{-1}), Equations 7-9 can be simplified as Equations 10-12 below:

$[\text{MVKO}]_0 = \alpha[\text{MVKO}]_{\text{total}}$ $[\text{adduct}]_0 = (1-\alpha)[\text{MVKO}]_{\text{total}}$ (Equation 10)

$[\text{adduct}](t) = [\text{adduct}]_0 \exp(-k_r t)$ (Equation 11)

$$[\text{MVKO}](t) = [\text{MVKO}]_0 e^{-k_{obs}t} + [\text{adduct}]_0 \frac{k_r}{k_r - k_{obs}}[e^{-k_{obs}t} - e^{-k_r t}]$$

$$= [\text{MVKO}]_{\text{total}}\{\alpha e^{-k_{obs}t} + (1-\alpha)\frac{k_r}{k_r - k_{obs}}[e^{-k_{obs}t} - e^{-k_r t}]\}$$

(Equation 12)

$\Delta Abs = \sigma L[\text{MVKO}](t) + C_0.$ (Equation 13)

$k_{obs} = k_{SO2}[SO_2] + k_0$ (Equation 14)

where σ is the absorption cross section of MVKO at the probe wavelength, L is the

effective light path length (L = 71 x 6 = 426 cm), C_0 represents the baseline of the

absorption signal at long delay time. The result of fitting is shown in Figure 11.
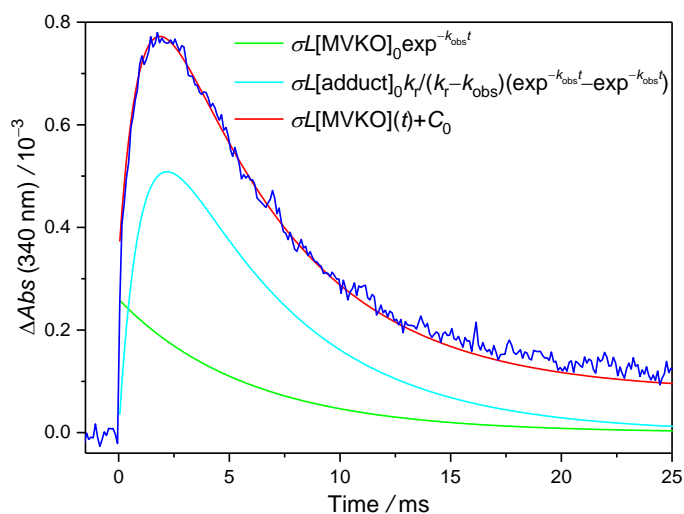
Figure 11. Time trace of MVKO absorption and its model fit at 102 Torr and 299 K. The probe wavelength is (340 ± 5) nm. The fitting range is 0.1-25 ms. The data is from Table 1, Exp K6a. Time zero is when the photolysis laser fired. Green and cyan curves show the fitting of promptly generated MVKO and the fitting of MVKO formed from the reaction of the adduct. The red curve is the sum of them.

During experiments for the reaction of MVKO with SO_2, we controlled the concentration of precursor and the laser fluence to be constant, and $[SO_2]$ was scanned up and down in one experimental set. From Equations 12-14, time trace of MVKO absorption can be fitted with six parameters, which are $\sigma L[MVKO]_{total}$, $(1-\alpha)$, k_r, k_{SO2}, k_0, and C_0. In the fitting, $\sigma L[MVKO]_{total}$, $(1-\alpha)$, k_r, k_{SO2}, k_0 were set as global parameters which were optimized for all traces in one experimental set, while C_0 was

26

treated as a local parameter optimized to fit each trace. (See Figure 12 for the fitting

result.) In this way, the parameters would not couple with one another.
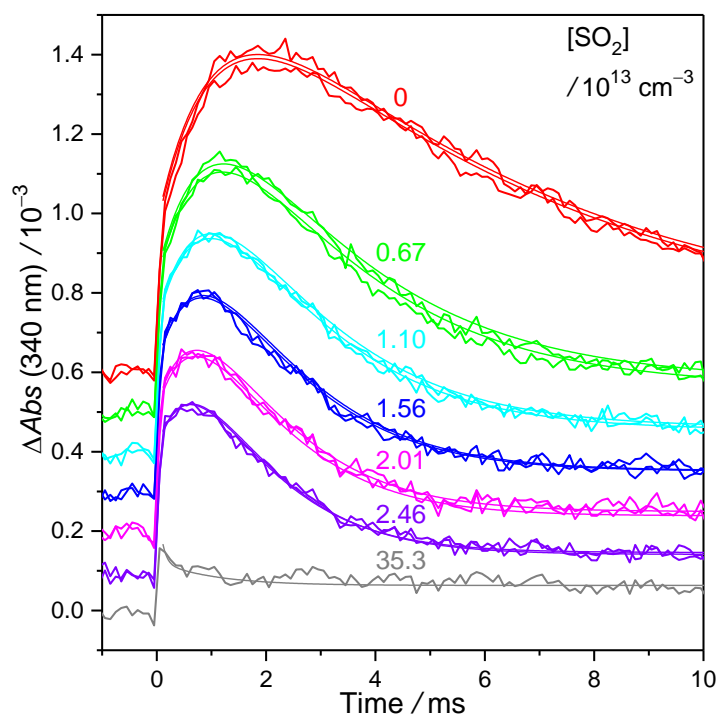
Figure 12. Time traces of MVKO under various [SO$_2$] at 102 Torr and 299 K. [SO$_2$] =

0-4 x 10^{14} cm^{-3}. The data are from Table 1, Exp K6a. The probe wavelength is (340±5)

nm. The fitting range is 0.1-25 ms. The laser pulse is set at time zero. Traces are

vertically shifted for clarity. With more SO$_2$, the signal of MVKO decays faster. The

curves represent the fitting results from Equation 12. Note that there are two traces for

each [SO$_2$] except for [SO$_2$] = 4 x 10^{14} cm^{-3} because we recorded MVKO traces by

scanning [SO$_2$] from 0 to maximum, then, back to 0. The stability of our system is good

because the traces at the same condition are similar.
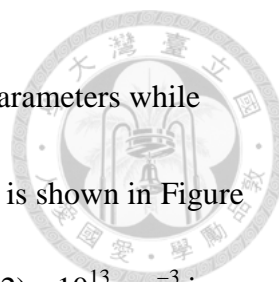
We also tried the "k_{obs} local fit", in which k_{obs} and C_0 are local parameters while

$\sigma L[MVKO]_{total}$, k_r, and $(1-\alpha)$ are set as global parameters. The result is shown in Figure

13. k_{obs} derived from the "k_{obs} local fit" with the data of $[SO_2] = (0\text{-}2.2) \times 10^{13}$ cm^{-3} is

4.2×10^{-11} cm^3 s^{-1}, which is similar to k_{obs} obtained from the global fit (4.24×10^{-11} cm^3

s^{-1}). However, k_{obs} obtained from the "k_{obs} local fit" would deviate to 3.7×10^{-11} cm^3 s^{-1}

if including the data of $[SO_2] = 4.4 \times 10^{13}$ cm^{-3}. The data of high $[SO_2]$ are less reliable

because of small signal. (see Figure 13).
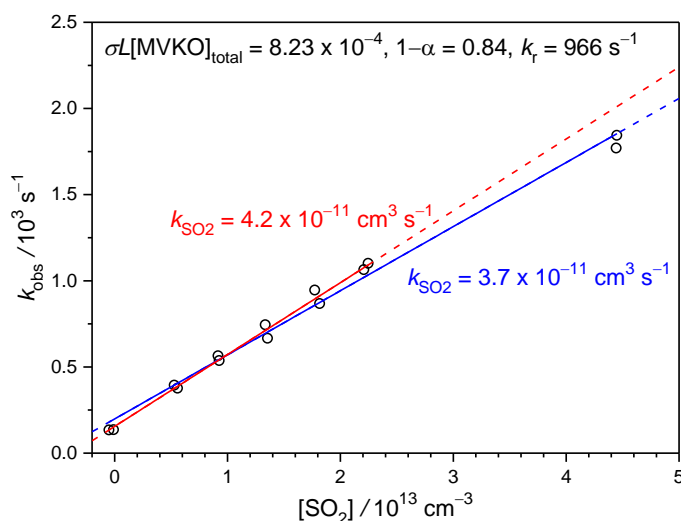
Figure 13. The observed decay rate coefficient, k_{obs}, from the "k_{obs} local fit" as a

function of $[SO_2]$. The data are from Exp K8a in Table 1. "k_{obs} local fit" means k_{obs} and

C_0 are set as local parameters while $\sigma L[MVKO]_{total}$, k_r, and $(1-\alpha)$ are set as global

parameters. The solid lines show the range of linear regression, and the dash lines

indicated the extension of solid lines. The slope of the linear regression in the range of

$[SO_2] = (0\text{-}2.2) \times 10^{13}$ cm^{-3} (red line) is close to the result from the global fit (k_{SO2} = 4.24×10^{-11} cm^3 s^{-1}). However, for the linear regression including data of $[SO_2]$ = 4.4 x 10^{13} cm^{-3}, k_{SO2} is 3.7×10^{-11} cm^3 s^{-1}. k_{obs} obtained from higher $[SO_2]$ could be less reliable due to smaller signal (see Figure 12).

3.3 Results

3.3.1 Results at 298 K and 4-703 Torr

The results of the reaction of MVKO with SO$_2$ at 298 K and 4-703 Torr are shown in Figure 14 and Table 1. From the upper panel of Figure 14, we conclude that the reaction rate coefficient, k_{SO2} is independent on the total pressure at 4-703 Torr, and k_{SO2} = $(4.0\pm0.6) \times 10^{-11}$ cm^3 s^{-1} at 298 K. The relationship between the adduct yield, $(1-\alpha)$, and the total pressure is shown in the middle panel of Figure 14. The yield increases sharply from 4 to 101 Torr, and remains nearly a constant (~0.8) for 101-703 Torr. The lower panel of Figure 14 represents the reaction rate coefficient of CH$_3$(C$_2$H$_3$)ClOO $\rightarrow$ CH$_3$(C$_2$H$_3$)COO + I, k_r, plotted against the total pressure. Note that for P < 100 Torr, the concentration of adduct is small and the observed k_r is less reliable. At P = 101-703 Torr, k_r shows an insignificant pressure effect.

We believe the error of the measured reaction rate coefficient of MVKO with SO$_2$ is mainly from the error of $[SO_2]$. The error of the literature cross section of SO$_2$ is 5-10

29
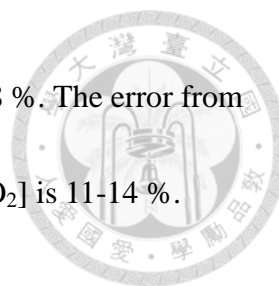
%,[30] and the error from gas mixing and pressure change is less than 8 %. The error from the baseline of the spectrum is ~5 %. Therefore, the total error of [SO_2] is 11-14 %.
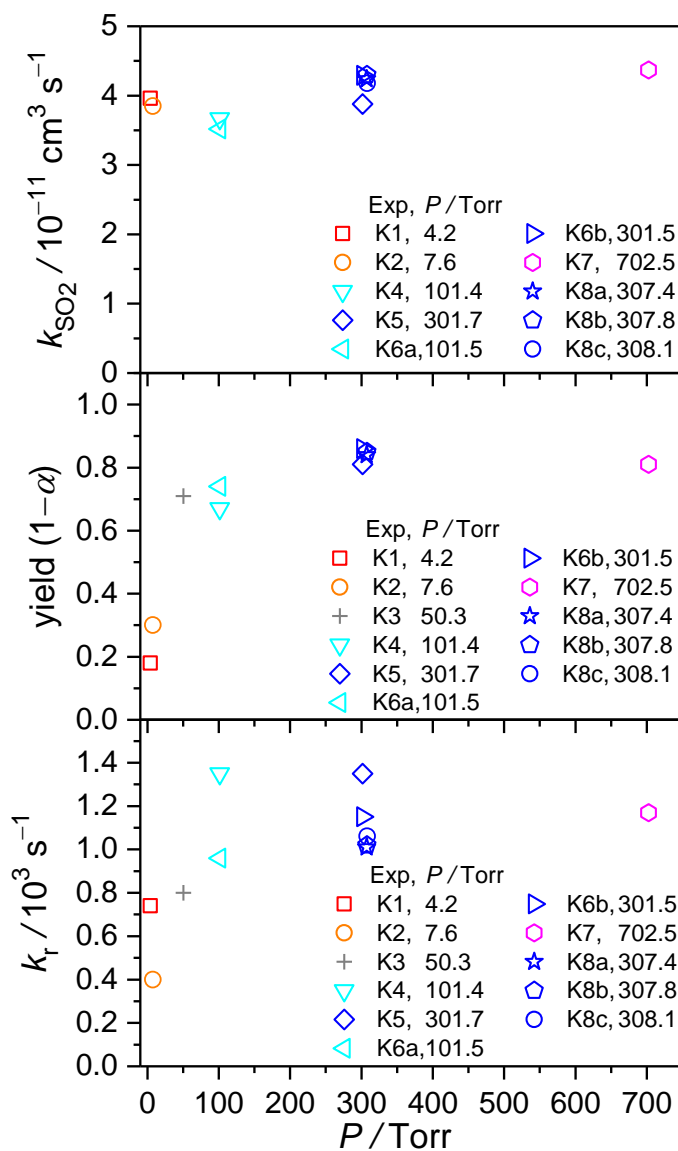
Figure 14. Plot of fitting parameters, k_{SO2}, adduct yield $(1-\alpha)$, and k_r, as a function of the total pressure.
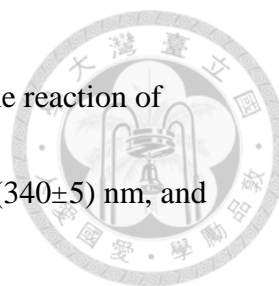
Table 1. Summary of experimental conditions and fitting results of the reaction of MVKO with SO_2 at 298 K and 4-703 Torr. The probe wavelength is (340±5) nm, and the fitting range is 0.1-25 ms.

Exp No.	Abs_{prec} [a]	P_{O2} / Torr	P_{total} [b] / Torr	I [c] / mJ cm^{-2}	σL[MVKO]$_{total}$ / 10^{-3}	$1-\alpha$	k_r / 10^3 s^{-1}	k_{SO2} / 10^{-11} cm^3 s^{-1}	k_0 / s^{-1}
K1	0.028	4.0	4.2	5.89	2.35	0.18	0.74	4.0	207
K2	0.122	7.5	7.6	2.95	3.86	0.30	0.40	3.9	235
K3	0.063	10.2	50.3	1.02	0.82	0.71	0.80	3.1[d]	95
K4	0.108	67.6	101.4	5.89	4.41	0.67	1.35	3.7	232
K5	0.108	65.2	301.7	5.89	4.95	0.81	1.35	3.9	247
K6a	0.024	10.3	101.5	3.93	1.00	0.74	0.96	3.5	172
K6b	0.024	10.1	301.5	1.96	0.64	0.86	1.15	4.3	118
K7	0.012	10.2	702.5	3.93	1.15	0.81	1.17	4.4	130
K8a	0.019	10.4	307.4	3.93	0.81	0.84	1.01	4.2	135
K8b	0.019	10.4	307.8	3.93	0.80	0.85	1.02	4.3	124
K8c	0.018	10.4	308.1	3.93	0.76	0.86	1.06	4.2	128

[a] The concentration of precursor is represented by its absorbance in the reactor ($L = 71 \times 6 = 426$ cm) at 238.5 nm due to lack of its absolute cross section.

[b] Balanced by N_2.

[c] I denotes laser fluence.

[d] k_{SO2} has large uncertainty because the [SO_2] used in this experiment was too high.

3.3.2 Results at 278-319 K and 302 Torr

Figure 15 shows the Arrhenius plots of k_{SO2} and k_r at 302 Torr and 278-319 K. k_{SO2} has a negative temperature dependence, and the activation energy is (-3.1 ± 0.8) kcal mol^{-1}. k_r is larger at higher temperature, and the activation energy is (14.0 ± 0.9) kcal mol^{-1}.
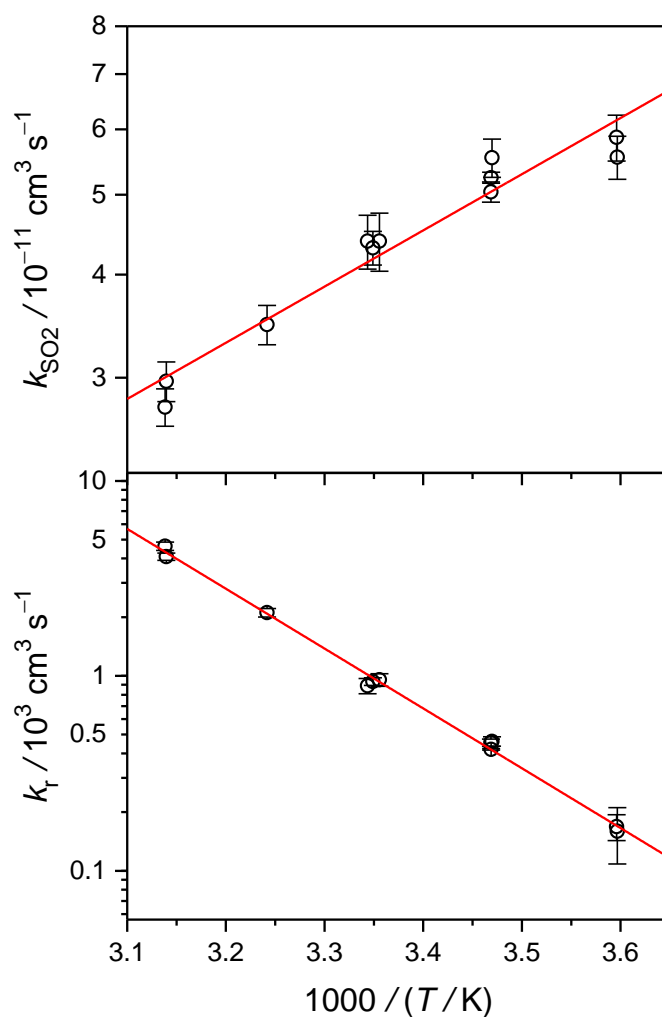
Figure 15. Arrhenius plots of k_{SO2} and k_r at 302 Torr and 278-319 K (Table 5, Exp 1-11).

The y-axis is in $\log_{10}$ scale. The activation energy for k_{SO2} is (-3.1 ± 0.8) kcal mol^{-1} while that for k_r is (14.0 ± 0.9) kcal mol^{-1}.

32

3.4 Discussion

3.4.1 MVKO conformer distribution

MVKO has four possible conformers, and Barber *et al*. reported the IR action

spectrum of all conformers.[4] However, in our experimental results, the time trace of

MVKO absorption signal could be fitted well by considering only one kind of decay

behavior. The unimolecular decomposition rate coefficient of *anti*-MVKO has been

predicted to be 2140 s^{-1} or 13400 s^{-1},[4, 5] which should be observable in our system but

we did not observe it. As for *syn*-MVKO, the unimolecular decomposition rate

coefficient has been predicted to be 33 s^{-1} or 50 s^{-1},[4, 5] and the interconvert rate

coefficient between *syn-trans*-MVKO and *syn-cis*-MVKO has been reported to be 2.4

x 10^7 s^{-1} by theoretical calculations.[5] Therefore, the possible explanations of our result

are that the yield of stabilized *anti*-MVKO is low or the unimolecular decomposition

rate coefficient of *anti*-MVKO is larger than the previous prediction. Thus, we only

observed *syn*-MVKO in our system. The difference between our thermal stabilized

condition and the jet-cooled condition of Barbel *et al*.[4] is the possible reason why they

observe all four conformers of MVKO but we only observe *syn*-MVKO. The

temperature could affect the Boltzmann distribution as well as the reactivity of MVKO,

and thus the conformer distribution.
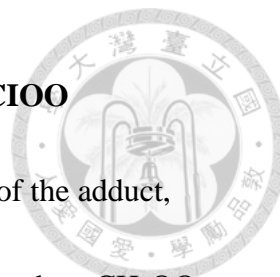
3.4.2 The comparison between adducts: CH_2IOO *vs.* $CH_3(C_2H_3)CIOO$

We observed a slow formation of MVKO caused by the reaction of the adduct, $CH_3(C_2H_3)CIOO$ in our system. For a smaller Criegee intermediate, such as CH_2OO, an adduct would also be generated by the reaction of O_2 with an iodo-alkyl radical ($CH_2I + O_2 \rightarrow CH_2IOO$). However, CH_2IOO would not turn into CH_2OO in our observation time (≤ 0.1 s). At higher pressure, the yield of CH_2IOO would increase, and that of CH_2OO would decrease.[31, 32]

We believe that for the case of $CH_3(C_2H_3)CIOO$, both the iodo-alkenyl radical ($CH_3(C_2H_3)CI$) and $CH_3(C_2H_3)COO$ are resonance-stabilized. Therefore, it is easier for the reaction of $CH_3(C_2H_3)CIOO \rightarrow CH_3(C_2H_3)COO + I$ to happen. The calculated relative energies ΔH and equilibrium constants K_{eq} for MVKO + I and CH_2OO + I system has been reported by Lin *et al*.[33] (See Table 2 and Figure 16) The calculated relative energy between $CH_3(C_2H_3)CIOO$ and $CH_3(C_2H_3)COO + I$ (ΔH (0 K) = 14.0 kcal mol^{-1}) are smaller than that between CH_2IOO and CH_2OO + I (ΔH (0 K) = 27.3 kcal mol^{-1}).[33] Thus, the equilibrium constant K_{eq} for $CH_3(C_2H_3)COO + I \rightarrow CH_3(C_2H_3)CIOO$ is smaller than that for $CH_2OO + I \rightarrow CH_2IOO$ by 10 orders of magnitude. The activation energy of k_r from our experiment is similar to the calculated relative energy between $CH_3(C_2H_3)CIOO$ and $CH_3(C_2H_3)COO + I$, our results are hence supported by this calculation.

34

Table 2. Calculated relative energies ΔH and equilibrium constants K_{eq} for MVKO + I

and CH$_2$OO + I systems. Calculation is performed by Dr. Kaito Takahashi (adapter from

Lin *et al.*[33]).

reaction	ΔH (0 K)[a] / kcal mol^{-1}	K_{eq} (298 K)[b] / cm^3	typical concentration / cm^{-3}	[adduct] / [coreactant][c]
CH$_2$I + O$_2$ → CH$_2$IOO	−26.4	3.91x10^{-8}	[O$_2$] = 3x10^{17}	1.2x10^{10}
CH$_2$OO + I → CH$_2$IOO	−27.3	1.85x10^{-5}	[I] = 3x10^{11}	5.6x10^6
CH$_3$(C$_2$H$_3$)CI + O$_2$ → CH$_3$(C$_2$H$_3$)CIOO	−15.5	1.26x10^{-16}	[O$_2$] = 3x10^{17}	38
CH$_3$(C$_2$H$_3$)COO + I → CH$_3$(C$_2$H$_3$)CIOO	−14.0	1.42x10^{-15}	[I] = 3x10^{11}	4.3x10^{-4}

[a] At CCSD(T)-F12/VTZ-F12//B2PLYP-D3BJ/VTZ level with vibrational zero-point correction at B2PLYP-D3BJ/VTZ. A spin-orbit correction of 7.24 kcal mol^{-1} was included for I atom.

[b] For example, K_{eq} = [CH$_2$IOO] / ([CH$_2$I][O$_2$]). The calculation is with the CCSD(T)-F12b energies and the partition functions calculated at B2PLYPDBJ/VTZ level with harmonic oscillator-rigid rotor approximation.

[c] [coreactant] means [CH$_2$I], [CH$_2$OO], [CH$_3$(C$_2$H$_3$)CI] or [MVKO], from the top row down.
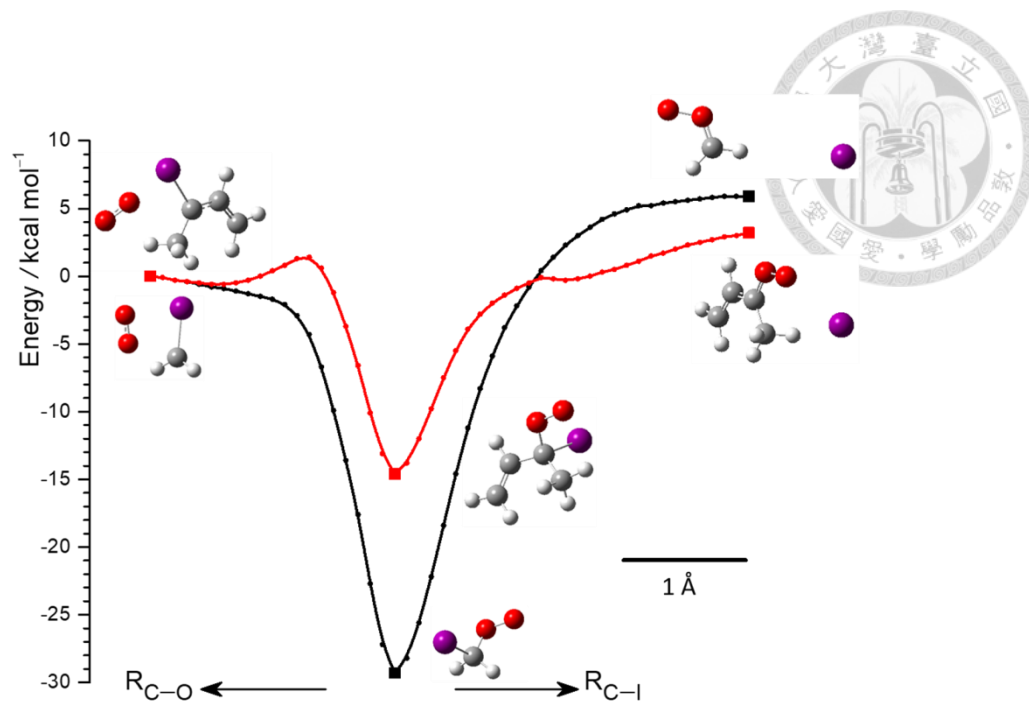
Figure 16. The calculated effective potential energy curves, at B3LYP-D3BJ/VTZ level, along the C−I and C−O bonds for the $CH_2OO + I$ (black) and MVKO + I (red) systems. The zero of the energy is taken at $CH_2I + O_2$ and $CH_3(C_2H_3)CI + O_2$, respectively. Calculation is performed by Dr. Kaito Takahashi (adapter from Lin et al.[33]). The corresponding energies of the plotted geometries are shown as square symbols. The spin-orbit correction for the iodine atom has not been added in this plot. Therefore, the energies at long C-I distances are over estimated.
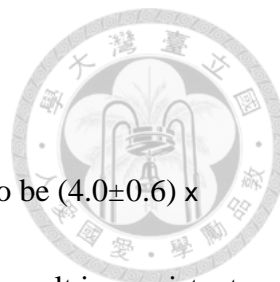
3.4.3 The reaction of Criegee intermediates with SO_2

The reaction rate coefficient of MVKO with SO_2 was measured to be (4.0 ± 0.6) x 10^{-11} cm^3 s^{-1} with an insignificant pressure effect at 4-703 Torr. This result is consistent with the rate coefficient reported by Caravan *et al*., which is (3.9 ± 0.5) x 10^{-11} cm^3 s^{-1} at 10 Torr with helium bath gas.[9] The reaction rate coefficients of small Criegee intermediates (CH_2OO, CH_3CHOO, $(CH_3)_2COO$) with SO_2 have been measured to be in the range of 10^{-10}-10^{-11} cm^3 s^{-1}.[11, 34-37] Thus, though MVKO has the resonance-stabilized structure, its observed reaction rate coefficient with SO_2 is similar to those of small Criegee intermediates. Also, we observed a negative temperature dependence of the reaction of MVKO with SO_2 at 278-319 K with the measured activation energy being (-3.1 ± 0.8) kcal mol^{-1}. The measured activation energy of MVKO + SO_2 is similar to that of $(CH_3)_2COO$ + SO_2 (-3.7 kcal mol^{-1}),[38] which means these two reactions might have similar mechanisms. A negative activation energy refers to a submerged transition state for the reaction. From the theoretical work of the reaction of small Criegee intermediates (CH_2OO, CH_3CHOO, and $(CH_3)_2COO$) with SO_2, the possible mechanism of the reaction is forming a five-membered-ring structure, going through a transition state, and decomposing to products.[39, 40] The energy of the transition state is higher than that of the five-membered-ring structure but lower than that of Criegee Intermediate with SO_2, which makes the transition state submerged.[39, 40]

37

The steady state concentration of all Criegee intermediates has been estimated to be ~10^4-10^5 cm^{-3} by Novelli *et al.*[41] To study the influences of the reactions of Criegee intermediates with SO_2 to the atmosphere, we assume that the reaction rate coefficient of Criegee intermediates with SO_2 is 4 x 10^{-11} cm^3 s^{-1}. The effective first-order rate coefficient of SO_2 oxidation by Criegee intermediates would be (0.4-4) x 10^{-6} s^{-1}. One of the main gaseous removal pathway for SO_2 in the atmosphere is by the reaction with OH radicals. The concentration of OH radicals is about (0-3.2) x 10^6 cm^{-3},[41] and the reaction rate coefficient of OH with SO_2 has been measured to be 1.3 x 10^{-12} cm^3 s^{-1} at 298 K.[42] Therefore, the effective first-order rate coefficient is (0-4.2) x 10^{-6} s^{-1}. The effective first-order rate coefficient of SO_2 reaction with Criegee intermediates is of the same order of magnitude as that of SO_2 reaction with OH radicals. The reaction with Criegee intermediates could be an important gaseous removal pathway for SO_2.

3.5 Conclusions

We generated MVKO by the reaction of O_2 with the iodo-alkenyl radical, and studied the reaction of MVKO with SO_2 at 4-703 Torr. We probed MVKO with its strong UV absorption at 340 nm.

Though MVKO has four possible conformers, our experimental results do not show any evidence of *anti*-MVKO, of which the unimolecular decay rate coefficient has

38

been predicted to be ~2000 s^{-1}.[4] This observation suggests that in our thermalized

system, the yield of *anti*-MVKO is very low or the decomposition rate coefficient of

anti-MVKO is much larger than the previous estimation,[4, 5] and we only observed the

kinetics of *syn*-MVKO.

We found a slow formation process of MVKO (1-2 ms) at high pressure (>100

Torr). This slow formation of MVKO is assumed to be from the decomposition of the

adduct ($CH_3(C_2H_3)CIOO \rightarrow CH_3(C_2H_3)COO + I$). The observed kinetics of MVKO

agree very well with the model considering this adduct mechanism. The activation

energy of the decomposition of the adduct was measured to be (14.0±0.9) kcal mol^{-1},

which is similar to the calculated relative energy between $CH_3(C_2H_3)CIOO$ and

$CH_3(C_2H_3)COO + I$.[33] The measured decay rate coefficient of the adduct shows no

significant pressure dependence at 101-703 Torr. The adduct yield was measured to be

significant (~0.8) at 101-703 Torr. This adduct mechanism is important for the study of

MVKO generated by the same method at near atmospheric conditions.

We also measured the reaction rate coefficient of MVKO with SO_2 to be (4.0±0.6)

x 10^{-11} cm^3 s^{-1} with an insignificant pressure effect at 4-703 Torr. The activation energy

of the reaction of MVKO with SO_2 was measured to be (−3.1±0.8) kcal mol^{-1}, which is

similar to that of $(CH_3)_2COO + SO_2$ (−3.7 kcal mol^{-1}).[38] A negative activation energy

would suggest a submerged transition state for the reaction, and the reaction of MVKO

+ SO$_2$ may have a mechanism similar to the reaction of (CH$_3$)$_2$COO + SO$_2$. The removal of SO$_2$ through the reaction with Criegee intermediates could be important in the atmosphere.
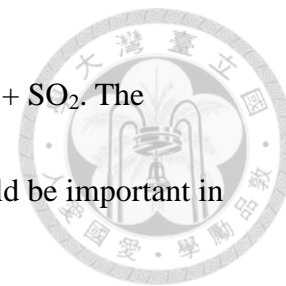
Chapter 4. Unimolecular Decomposition of MVKO

4.1 The reaction of MVKO at 278-319 K and 302 Torr

To study the unimolecular decomposition kinetics of MVKO, we did the experiments at different initial concentrations of MVKO. The concentration of MVKO was controlled by adjusting the concentration of the precursor and the photolysis laser fluence. To follow the analysis method in Chapter 3, we added SO$_2$ ([SO$_2$] ~ 10^{12} cm^{-3}) in the system. Adding SO$_2$ can clarify the kinetics of MVKO, and avoid coupling among fitting parameters by setting some parameters as global parameters. If we measure the decay rate of MVKO at various initial MVKO concentrations when there is no SO$_2$, our observation could involve some kinetics from byproducts and fitting parameters such as σL[MVKO]$_{total}$, k_{obs}, and C_0 would couple with one another. (See Chapter 3.2 for the meaning of fitting parameters) Thus, we believe with SO$_2$ present the result we get is more reliable. In a subset experiment, the laser fluence and the concentration of the precursor were controlled to be constant while [SO$_2$] was scanned. A set of experiment was comprised of subsets at different initial MVKO concentrations.

The experiments were conducted at 100-503 Torr and 278-319 K, and the detailed conditions are listed in Table 4-5.

The time traces of MVKO absorption signal under various [SO_2] at 301 Torr and 278-319 K are shown in Figure 17. The formation rate coefficient of MVKO from the adduct ($CH_3(C_2H_3)CIOO$) seems to be faster at higher temperature. We used the fitting model discussed in Chapter 3.2 to fit the time traces (Equation 12-14). To show the uncertainty of the fitting, we used the "k_{obs} local fit" here. (The k_{obs} local fit means k_{obs} and C_0 are set as local parameters while $\sigma L[MVKO]_{total}$, k_r, and $(1-\alpha)$ are set as global parameters.) The corresponding pseudo-first order plots are shown in Figure 18. The slope of the pseudo-first-order plot, denoted as k_{SO2}, indicates the reaction rate coefficient, and the intercept, denoted as k_0, represents the rate coefficient without SO_2. The results are shown in Table 4-5.

$$[MVKO](t) = [MVKO]_0 e^{-k_{obs}t} + [adduct]_0 \frac{k_r}{k_r - k_{obs}}[e^{-k_{obs}t} - e^{-k_r t}]$$

$$= [MVKO]_{total}\{\alpha e^{-k_{obs}t} + (1-\alpha)\frac{k_r}{k_r - k_{obs}}[e^{-k_{obs}t} - e^{-k_r t}]\}$$

(Equation 12)

$$\Delta Abs = \sigma L[MVKO](t) + C_0.$$ (Equation 13)

$$k_{obs} = k_{SO2}[SO_2] + k_0$$ (Equation 14)

$$k_0 = k_{uni} + k_{wall} + k_X[X]$$ (Equation 15)

where symbols are of the same meanings as in Chapter 3.2.
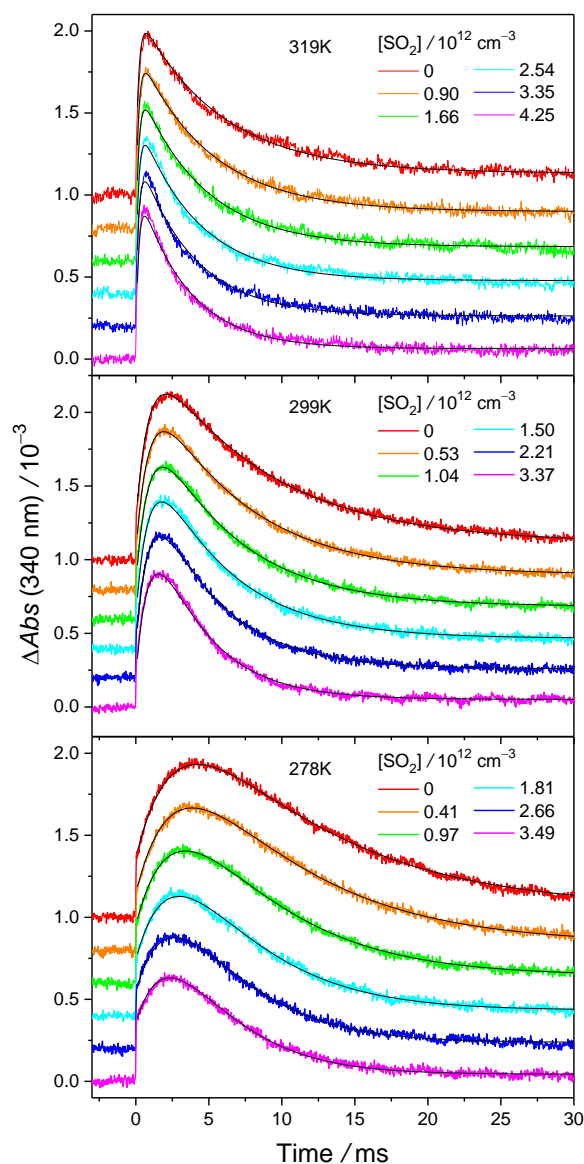
Figure 17. Time traces of MVKO under various [SO$_2$] at 301 Torr. (Table 5, Exp 1$_f$, 5$_c$,

and 10$_b$) The probe wavelength is (340±5) nm. The upper/middle/lower panels show the

traces at 319 K/299 K/278 K respectively. The traces are vertically shifted for clarity.

Black curves represent the fitting results from Equation 12. The fitting range is 0.1-30

ms.

42
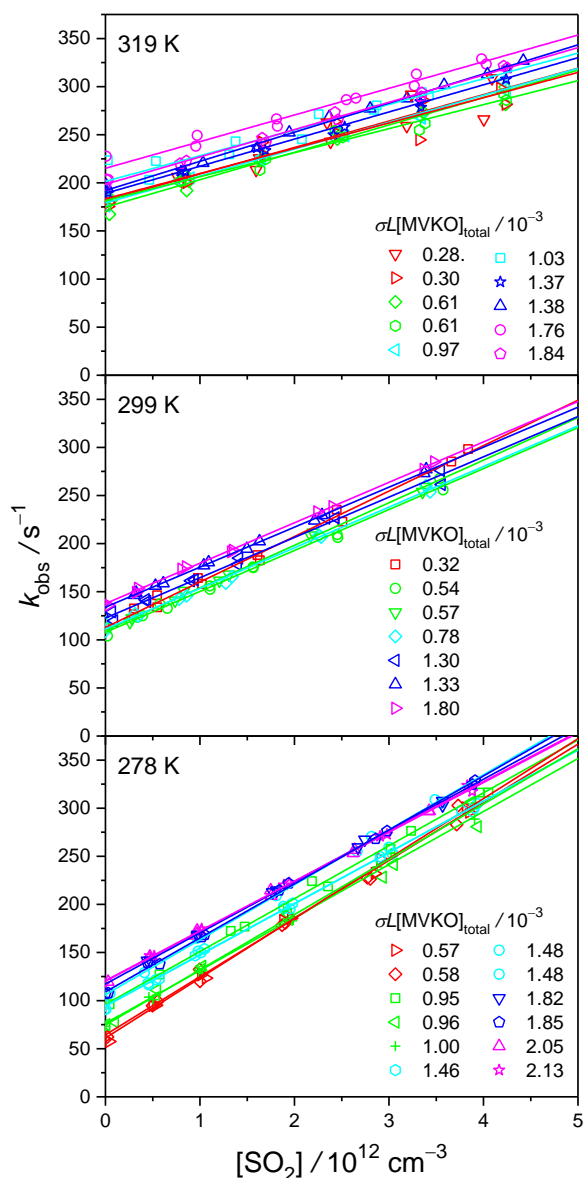
Figure 18. Pseudo-first-order plots of the reaction of MVKO with SO_2 at 301 Torr and

319 K/299 K/278 K (Table 5, Exp 1_f, 5_c, and 10_b). The different color symbols represent

the data at various concentration of MVKO. For the results at different temperature, the

data at lower temperature have larger slopes and smaller intercepts. For data under the

same conditions, the intercepts under higher concentrations of MVKO are higher.

43

4.2 Analysis

k_0 is composed of three parts: (1) unimolecular decomposition rate coefficient of MVKO, k_{uni}. (2) wall loss rate coefficient of MVKO, k_{wall}. (3) reaction rate coefficient of MVKO with other byproducts, $k_X[X]$. In our system, the radical byproducts, such as I, IO, and $CH_3(C_2H_3)CIOO$, etc., are proportional to $[MVKO]_{total}$ (See R1-R2 in Chapter 3.1). Therefore, we could remove the $k_X[X]$ term by plotting k_0 as a function of $\sigma L[MVKO]_{total}$, and the intercept of this plot would be $(k_{uni} + k_{wall})$. (See Figure 19)

$$k_0 = k_{uni} + k_{wall} + k_X[X] \tag{Equation 15}$$

where k_{uni} represents the unimolecular decomposition rate coefficient of MVKO, k_{wall} is the rate coefficient of the wall loss.
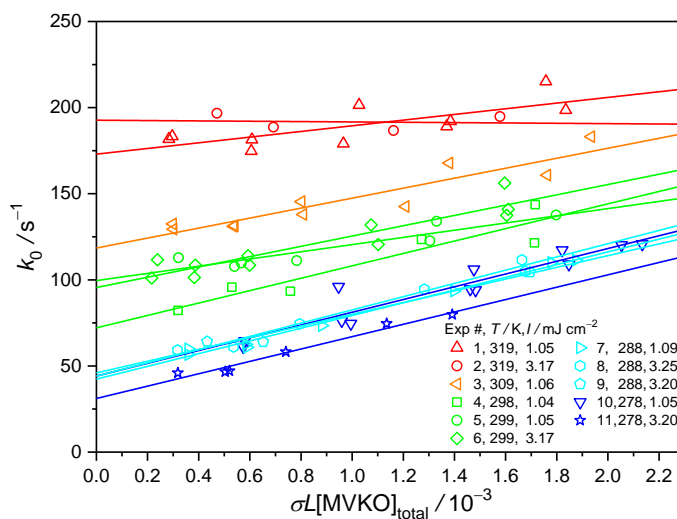
Figure 19. Plot of k_0 against $\sigma L[MVKO]_{total}$ at 302 Torr and 278-319 K. The laser fluence, denoted as I = 1.06 or 3.20 mJ cm^{-2}. (Table 4-5, Exp 1-11) The solid lines represent the linear regression of the data, and the lines with different colors indicate the

44
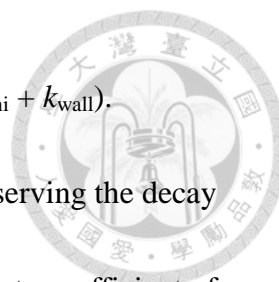
data at different temperature. The intercepts of this plot represent ($k_{uni} + k_{wall}$).

The wall loss rate coefficient of MVKO can be measured by observing the decay rate coefficient of CH_2OO because the unimolecular decomposition rate coefficient of CH_2OO has been reported to be quite small ((0.19 ± 0.07) s^{-1} by Berndt et al.[43]). We measured the decay rate coefficient of CH_2OO under different concentrations of the precursor at similar conditions to the experiments for the unimolecular decomposition of MVKO. The time traces of CH_2OO absorption signal at 301 Torr are shown in Figure 20, and the traces are fitted with the single exponential decay model, as Equation 16.

$$[CH_2OO](t) = [CH_2OO]_0 exp(-k_{obs}t) \qquad \text{(Equation 16)}$$
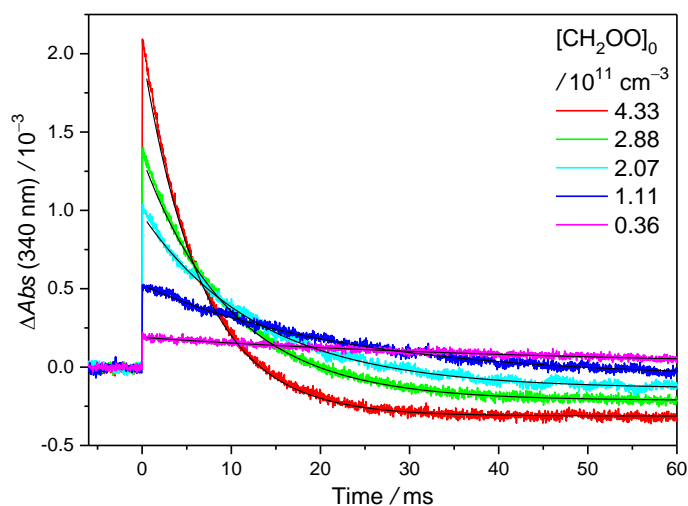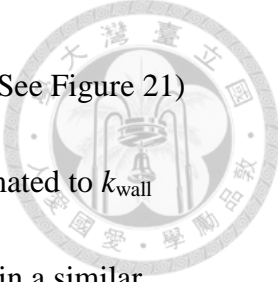
Figure 20. The time traces of the absorption signal of CH_2OO under various $[CH_2OO]_0$ at 301 Torr and 299 K. (Table 3, Exp F) The probe wavelength is (340 ± 5) nm. The black curves show the fitting results.

45

We plotted k_{obs} against $[CH_2OO]_0$ to remove the term of $k_X[X]$. (See Figure 21) The intercept of this plot is ($k_{wall} + k_{uni\_CH2OO}$), which can be approximated to k_{wall} because k_{uni_CH2OO} is quite small. Simulated diffusion loss of CH_2OO in a similar experimental system has been reported to be slow at 100-700 Torr, and gas turbulence has been thought to be the main cause of wall loss at high pressure.[44] Therefore, we believe the observed wall loss rate coefficient could also be explained by gas turbulence at our high pressure (100-503 Torr) experimental conditions. Because the concentrations of the precursor and Criegee intermediate are too low to affect gas turbulence, we believe the wall loss rate coefficient of CH_2OO is similar to that of MVKO. The measured wall loss rate coefficient has been reported to have small variations at 100-700 Torr and 278-350 K in a similar experimental system.[44] The measured wall loss rate coefficients in our system have no significant temperature dependence at 278-319 K; the rate coefficient is (7.8 ± 2.7) s^{-1} (See Figure 22 and Table 3).
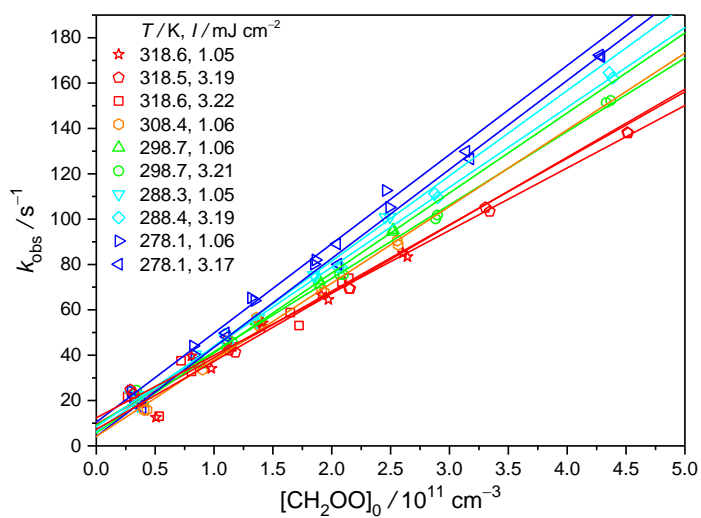
Figure 21. The plot of k_{obs} against $[CH_2OO]_0$ at 301 Torr and 278-319 K.
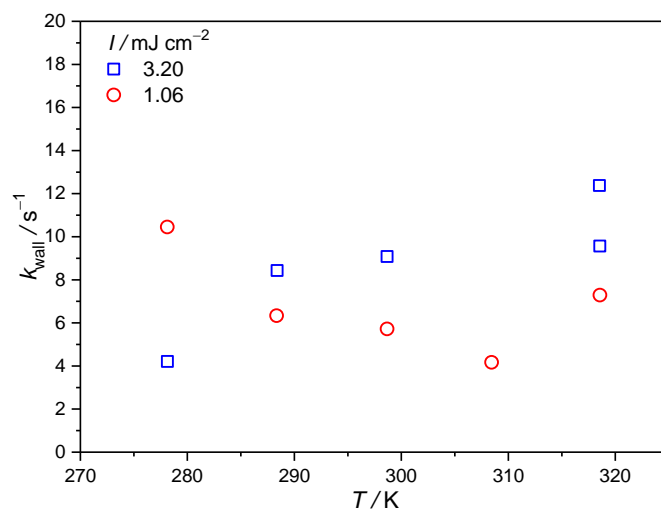
Figure 22. Plot of the wall loss rate coefficients against temperature at 301 Torr.

47
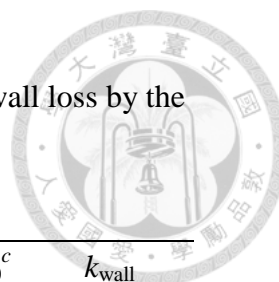
Table 3. Summary of experimental conditions and the results of the wall loss by the measurement of the kinetics of CH_2OO at 301 Torr and 278-319 K.

Exp #	P_{O2} / Torr	P_{total}[a] / Torr	T / K	I[b] / mJ cm^{-2}	$[CH_2OO]_0$[c] / 10^{11} cm^{-3}	k_{wall} / s^{-1}
A	11.0	302.2	318.6	1.05	0-2.6	7.3±11.2[d]
B	10.9	301.4	318.5	3.19	0-4.5	12.4±4.9
C	10.9	300.7	318.6	3.22	0-2.1	9.6±13.2
D	11.0	301.6	308.4	1.06	0-2.6	4.2±6.4
E	10.9	301.9	298.7	1.06	0-2.5	5.7±2.1
F	10.8	301.0	298.7	3.21	0-4.4	9.1±4.1
G	10.9	300.7	288.3	1.05	0-2.5	6.3±4.7
H	10.8	299.8	288.4	3.19	0-4.4	8.4±5.4
I	10.9	300.7	278.1	1.06	0-2.5	10.5±6.5
J	10.9	300.3	278.1	3.17	0-4.3	4.2±5.5

[a] Balanced by N_2.

[b] I represents laser fluence.

[c] $[CH_2OO]_0$ is calculated by Beer's law. The effective optical path is 426 cm, and the literature cross section of CH_2OO at our probe wavelength is 1.26 x 10^{-17} cm^2.[25]

[d] The average wall loss rate coefficient is (7.8 ± 2.7) s^{-1}; the error is one standard deviation of k_{wall}.

4.3 Results

We obtained the unimolecular decomposition rate coefficient of MVKO after subtracting k_{wall} from ($k_{uni} + k_{wall}$). (See Table 4) The measured unimolecular decomposition rate coefficient is (81±15) s^{-1} at 299 K and 301 Torr, which is in the same order of magnitude as the calculated unimolecular decomposition rate coefficient of *syn*-MVKO (33 s^{-1} at 298 K) reported by Barber *et al.*[4] The Arrhenius plot of the unimolecular decomposition rate coefficient of MVKO is shown in Figure 23. The activation energy is (8.3±2.5) kcal mol^{-1}.
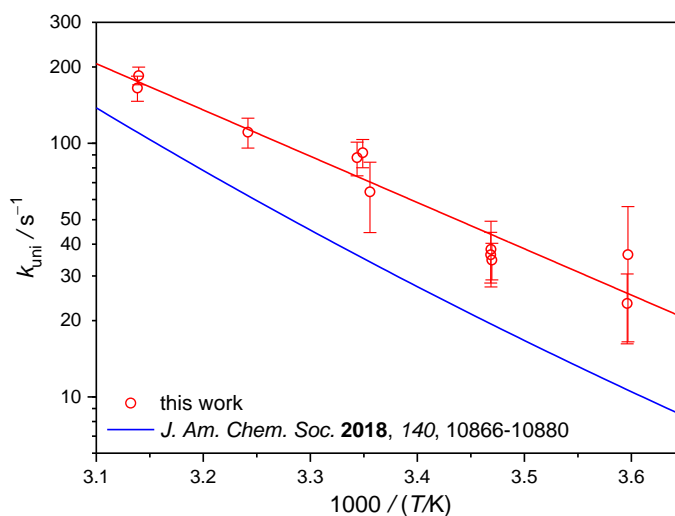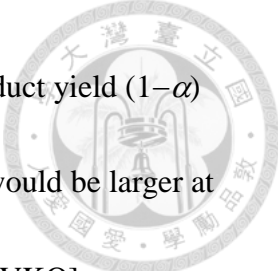
Figure 23. Arrhenius plot of the unimolecular decomposition rate coefficient of MVKO at 302 Torr. The y-axis is log$_{10}$ scale. The red circles represent results of this work. The solid blue line is the modified Arrhenius expression of *syn*-MVKO reported by Barber *et al.*[4]

The result of other fitting parameters such as k_r, k_{SO2}, and the adduct yield $(1-\alpha)$ are shown in Figure 24. The upper panel of Figure 24 indicates k_{SO2} would be larger at lower temperature. k_{SO2} seems have a negative correlation with $\sigma L[MVKO]_{total}$ especially at lower temperature. However, due to the slower formation rate from the adduct and the faster reaction rate with SO_2, the absorption signal of MVKO would be small at low temperature, and therefore the fitting result would be less reliable. The middle panel represents the adduct yield $(1-\alpha)$ at different temperature. The yield would be higher at higher temperature. The relationship of k_r with $\sigma L[MVKO]_{total}$ is shown in the lower panel of Figure 24. k_r is larger at higher temperature, and k_r seems have a positive correlation with $\sigma L[MVKO]_{total}$. The adduct could react with other radicals, such as I, IO, $CH_3(C_2H_3)COO$, and $CH_3(C_2H_3)CIOO$, etc. The concentrations of other radicals are proportional to $[MVKO]_{total}$; therefore, k_r seems larger at higher $\sigma L[MVKO]_{total}$.

50
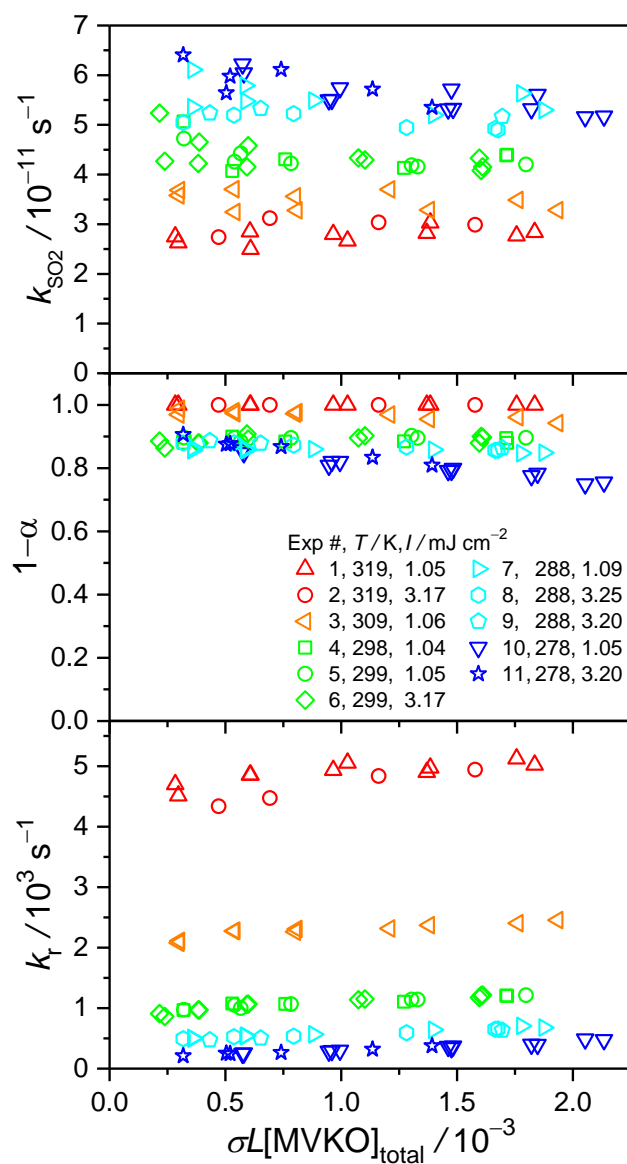
Figure 24. Plots of k_{SO_2}, the adduct yield $(1-\alpha)$, and k_r against $\sigma L[\text{MVKO}]_{total}$ at 302

Torr and 278-319 K. (Table 4. Exp 1-11)
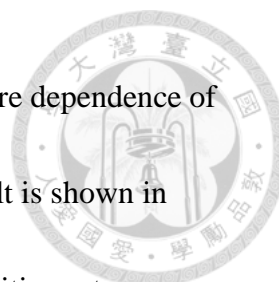
We did the experiments at different pressure to check the pressure dependence of

the unimolecular decomposition rate coefficient of MVKO. The result is shown in

Figures 25-26 and Tables 4-5. The measured unimolecular decomposition rate

coefficient of MVKO is (71 ± 18) s^{-1} at 299 K and 100-503 Torr with an insignificant

pressure dependence.
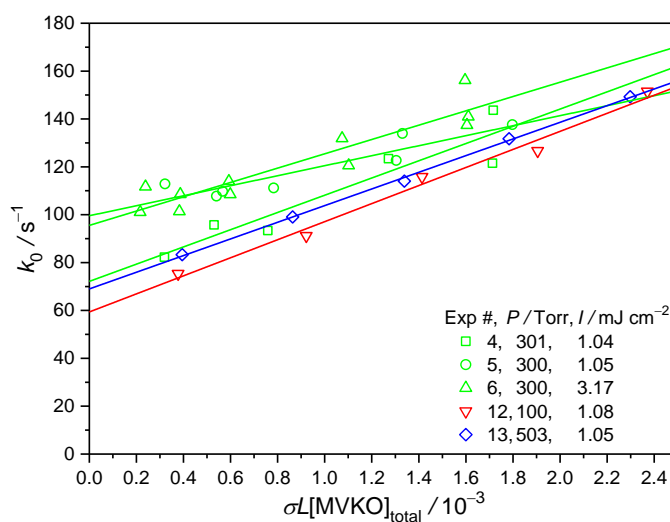
Figure 25. Plot of k_0 against σL[MVKO]$_{total}$ at 299 K and 100-503 Torr. The solid lines

represent the linear regression of the data, and the lines with different colors indicate the

data at different pressure. (Table 4-5, Exp 4-6, 12-13.)
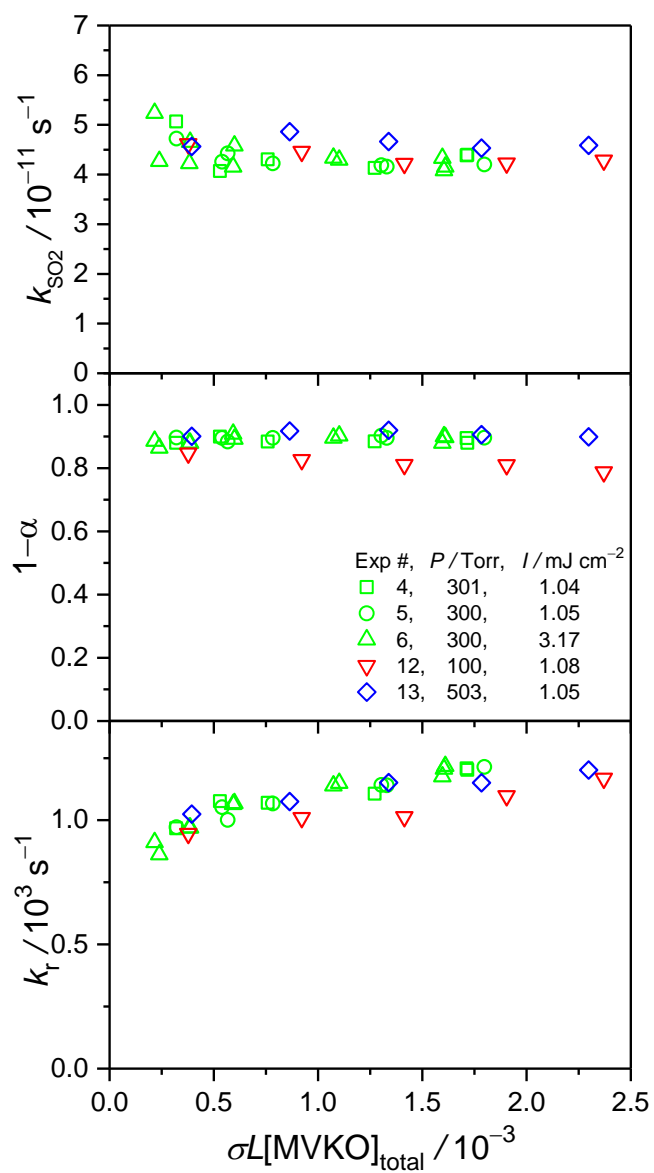
Figure 26. Plot of k_{SO2}, the adduct yield $(1-\alpha)$, and k_r as functions of $\sigma L[\text{MVKO}]_{total}$ at 299 K and 100-503 Torr.
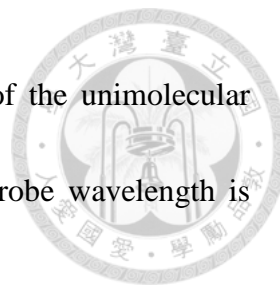
Table 4. Summary of experimental conditions and fitting results of the unimolecular decomposition of MVKO at 100-503 Torr and 278-319 K. The probe wavelength is (340±5) nm. The fitting time range is 0.1-30 ms.

Exp #	P_{total}[a] / Torr	T / K	I[b] / mJ cm^{-2}	k_{SO2} / 10^{-11} cm^3 s^{-1}	$(k_{uni} + k_{wall})$ / s^{-1}	k_{uni} / s^{-1}
1	302.6	318.6	1.05	2.8±0.14[c]	173±19[d]	165±19[e]
2	301.8	318.5	3.17	3.0±0.16	193±15	185±15
3	303.9	308.5	1.06	3.5±0.19	119±15	111±15
4	301.4	298.0	1.04	4.4±0.36	72±20	64±20
5	299.8	298.6	1.05	4.3±0.20	100±11	92±12
6	300.4	299.1	3.17	4.4±0.33	96±13	88±13
7	300.7	288.2	1.09	5.5±0.30	42±5	35±6
8	301.7	288.3	3.25	5.0±0.14	44±8	36±8
9	303.7	288.3	3.20	5.2±0.08	46±11	38±11
10	300.8	278.0	1.05	5.6±0.33	44±20	36±20
11	300.6	278.1	3.20	5.9±0.38	31±7	23±7
12	100.2	298.2	1.08	4.4±0.17	59±9	52±10
13	502.5	298.6	1.05	4.6±0.13	69±2	61±4

[a] Balanced by N_2.

[b] I represents laser fluence.

[c] The average of reaction rate coefficients of MVKO with SO_2 in an experimental subset; the error is one standard deviation

[d] The error bar is one standard deviation of $(k_{uni} + k_{wall})$.

[e] $\sigma_{k_{uni}}^2 = \sigma_{(k_{uni}+k_{wall})}^2 + \sigma_{k_{wall}}^2$.
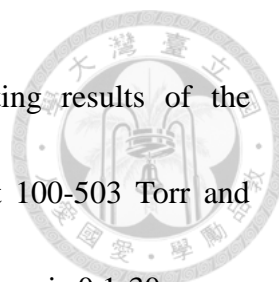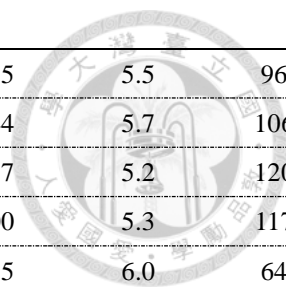
Table 5. Summary of the experimental conditions and the fitting results of the unimolecular decomposition of MVKO of experimental subsets at 100-503 Torr and 278-319 K. The probe wavelength is (340±5) nm. The fitting time range is 0.1-30 ms.

Exp #	T / K	Abs_{prec}[a]	P_{O2} / Torr	P_{total}[b] / Torr	I[c] / mJ cm^{-2}	$\sigma L[MVKO]_{total}$ / 10^{-3}	$1-\alpha$	k_r / s^{-1}	k_{SO2} / 10^{-11} cm^3 s^{-1}	k_0 / s^{-1}
1_a	318.7	0.075	10.9	302.2	1.06	1.03	1.00	5055	2.7	202
1_b	318.7	0.128	10.9	302.9	1.04	1.76	1.00	5124	2.8	215
1_c	318.7	0.100	10.9	302.8	1.05	1.38	1.00	4974	3.0	192
1_d	318.6	0.022	10.9	302.3	1.05	0.28	1.00	4698	2.7	182
1_e	318.6	0.047	10.9	302.4	1.03	0.61	1.00	4856	2.8	175
1_f	318.6	0.075	10.9	302.6	1.03	0.97	1.00	4935	2.8	179
1_g	318.6	0.025	10.9	302.2	1.06	0.30	1.00	4513	2.6	183
1_h	318.6	0.048	10.9	302.4	1.05	0.61	1.00	4856	2.5	181
1_i	318.6	0.104	10.9	302.9	1.04	1.37	1.00	4902	2.8	189
1_j	318.6	0.132	10.9	303.1	1.08	1.84	1.00	5020	2.8	199
2_a	318.5	0.041	10.9	301.9	3.18	1.58	1.00	4944	3.0	195
2_b	318.5	0.030	10.9	301.9	3.18	1.16	1.00	4838	3.0	187
2_c	318.5	0.019	10.9	301.7	3.17	0.69	1.00	4473	3.1	189
2_d	318.5	0.013	10.9	301.6	3.16	0.47	1.00	4338	2.7	197
3_a	308.5	0.134	11.0	303.5	1.05	1.93	0.94	2456	3.3	183
3_b	308.5	0.095	11.0	303.6	1.06	1.38	0.95	2370	3.3	168
3_c	308.5	0.056	11.0	303.5	1.07	0.80	0.97	2262	3.6	145
3_d	308.5	0.040	11.0	303.6	1.06	0.54	0.98	2273	3.7	131
3_e	308.5	0.025	11.0	303.7	1.07	0.30	0.97	2077	3.6	133
3_f	308.5	0.043	11.0	304.0	1.06	0.54	0.97	2276	3.2	132
3_g	308.5	0.027	11.0	303.9	1.06	0.30	0.99	2112	3.7	129
3_h	308.5	0.063	11.0	304.3	1.05	0.81	0.98	2306	3.3	138
3_i	308.4	0.091	11.0	304.5	1.05	1.21	0.97	2315	3.7	143
3_j	308.4	0.131	11.0	304.8	1.04	1.76	0.96	2404	3.5	161
4_a	298.0	0.139	10.9	301.2	1.04	1.72	0.88	1203	4.4	144
4_b	298.0	0.099	10.9	301.1	1.05	1.27	0.88	1106	4.1	123
4_c	298.0	0.056	10.9	301.0	1.05	0.76	0.88	1070	4.3	93
4_d	298.0	0.039	10.9	301.6	1.03	0.53	0.90	1077	4.1	96
4_e	298.0	0.025	10.9	301.6	1.03	0.32	0.88	967	5.1	82

55

4_f	298.0	0.137	10.9	302.3	1.01	1.71	0.89	1208	4.4	122
5_a	298.6	0.025	10.9	299.6	1.04	0.32	0.90	972	4.7	113
5_b	298.6	0.042	10.8	299.7	1.03	0.54	0.90	1052	4.3	108
5_c	298.6	0.099	10.9	300.1	1.06	1.33	0.90	1141	4.2	134
5_d	298.6	0.039	10.9	299.6	1.06	0.57	0.88	1001	4.4	110
5_e	298.6	0.055	10.9	299.6	1.05	0.78	0.90	1067	4.2	111
5_f	298.6	0.094	10.8	299.8	1.05	1.30	0.90	1142	4.2	123
5_g	298.6	0.132	10.8	300.1	1.04	1.80	0.90	1215	4.2	138
6_a	298.9	0.040	10.9	300.0	3.17	1.60	0.88	1175	4.3	156
6_b	298.9	0.028	10.9	300.1	3.15	1.07	0.90	1139	4.3	132
6_c	299.0	0.017	10.9	300.2	3.14	0.60	0.89	1068	4.6	109
6_d	299.1	0.012	10.9	300.2	3.20	0.38	0.88	970	4.2	101
6_e	299.1	0.010	10.9	300.3	3.18	0.24	0.86	862	4.3	112
6_f	299.1	0.014	10.9	300.5	3.17	0.39	0.88	969	4.7	109
6_g	299.1	0.011	10.9	300.5	3.19	0.22	0.89	911	5.2	101
6_h	299.1	0.021	10.9	300.6	3.17	0.59	0.91	1064	4.2	114
6_i	299.2	0.047	10.9	300.8	3.15	1.61	0.90	1217	4.2	141
6_j	299.2	0.035	10.9	300.7	3.15	1.10	0.90	1149	4.3	121
6_k	299.1	0.048	10.9	300.7	3.14	1.60	0.90	1207	4.1	137
7_a	288.2	0.135	11.3	301.1	1.07	1.78	0.85	706	5.6	110
7_b	288.2	0.137	11.3	300.9	1.08	1.88	0.85	678	5.3	111
7_c	288.2	0.099	11.3	300.8	1.09	1.40	0.86	642	5.2	94
7_d	288.2	0.060	11.3	300.6	1.09	0.88	0.86	566	5.5	73
7_e	288.3	0.041	11.3	300.5	1.09	0.59	0.86	543	5.5	61
7_f	288.2	0.026	11.3	300.5	1.10	0.36	0.86	499	6.1	57
7_g	288.2	0.043	11.3	300.7	1.10	0.59	0.86	540	5.8	63
7_h	288.2	0.028	11.3	300.6	1.09	0.36	0.86	506	5.4	60
8_a	288.3	0.045	10.9	301.6	3.20	1.66	0.86	649	4.9	112
8_b	288.2	0.034	10.9	301.6	3.23	1.28	0.87	593	4.9	95
8_c	288.3	0.022	10.9	301.6	3.25	0.79	0.87	538	5.2	74
8_d	288.3	0.017	10.9	301.6	3.27	0.54	0.88	526	5.2	61
8_e	288.3	0.012	10.9	301.7	3.26	0.32	0.88	493	5.0	59
8_f	288.3	0.050	10.9	302.0	3.25	1.68	0.86	655	4.9	105
9_a	288.3	0.045	11.0	303.7	3.20	1.70	0.86	634	5.2	104
9_b	288.3	0.016	11.0	303.7	3.20	0.65	0.88	504	5.3	64
9_c	288.3	0.012	11.0	303.7	3.19	0.43	0.89	473	5.2	64

10_a	278.1	0.077	10.9	299.6	1.06	0.95	0.81	285	5.5	96
10_b	278.1	0.130	10.9	300.5	1.06	1.48	0.79	344	5.7	106
10_c	278.0	0.219	10.9	301.2	1.04	2.05	0.75	487	5.2	120
10_d	278.0	0.174	10.9	301.0	1.04	1.82	0.78	400	5.3	117
10_e	278.1	0.043	10.9	300.1	1.05	0.58	0.85	255	6.0	64
10_f	278.0	0.080	10.9	300.5	1.04	0.96	0.82	296	5.5	76
10_g	278.0	0.044	10.9	300.3	1.03	0.57	0.86	249	6.2	61
10_h	278.0	0.134	10.9	300.9	1.05	1.46	0.79	364	5.3	95
10_i	278.0	0.223	10.9	301.6	1.04	2.13	0.76	477	5.2	121
10_j	278.0	0.178	10.9	301.4	1.03	1.85	0.78	398	5.6	109
10_k	278.0	0.136	10.9	301.1	1.06	1.48	0.80	372	5.3	94
10_l	278.0	0.082	10.9	300.8	1.06	0.99	0.82	303	5.7	75
11_a	278.0	0.046	10.9	300.4	3.18	1.39	0.81	378	5.4	80
11_b	278.1	0.035	10.9	300.6	3.20	1.13	0.83	319	5.7	75
11_c	278.1	0.022	10.9	300.6	3.20	0.74	0.87	265	6.1	58
11_d	278.1	0.016	10.9	300.6	3.21	0.52	0.88	247	6.0	47
11_e	278.1	0.012	10.9	300.7	3.22	0.32	0.91	210	6.4	46
11_f	278.1	0.018	10.9	300.8	3.21	0.50	0.88	252	5.6	47
12_a	297.9	0.175	10.8	99.8	1.08	2.37	0.79	1169	4.3	152
12_b	298.1	0.104	10.8	100.2	1.09	1.41	0.81	1013	4.2	116
12_c	298.3	0.143	10.8	100.4	1.08	1.90	0.81	1098	4.2	127
12_d	298.4	0.075	10.8	100.3	1.08	0.92	0.83	1010	4.5	91
12_e	298.4	0.041	10.8	100.3	1.08	0.38	0.85	946	4.6	75
13_a	298.6	0.159	10.7	503.0	1.05	2.30	0.90	1202	4.6	149
13_b	298.6	0.121	10.7	502.7	1.05	1.78	0.91	1151	4.5	132
13_c	298.6	0.090	10.7	502.5	1.05	1.34	0.92	1152	4.7	114
13_d	298.6	0.059	10.7	502.3	1.05	0.86	0.92	1075	4.9	99
13_e	298.6	0.026	10.7	501.9	1.04	0.39	0.90	1024	4.6	83

[a] The concentration of precursor is represented by its absorbance in the reactor ($L =$

71x6 = 426 cm) at 238.5 nm due to lack of its absolute cross section.

[b] Balanced by N_2.

[c] I represents the laser fluence.

4.4 Unknown species

Because the kinetics of MVKO with SO_2 would end within 30 ms, we did not consider the behavior of the absorption signal at longer delay time. However, as shown in Figure 27, we can see that there is a very slow decay signal at decay time longer than 30 ms for MVKO data at $T = 319$ K.
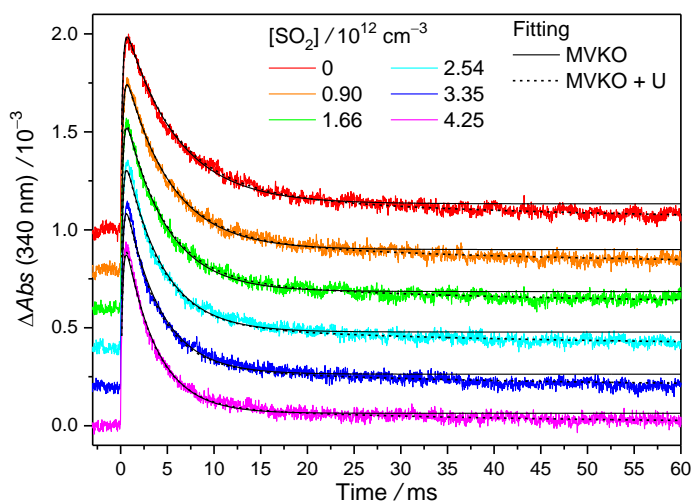
Figure 27. The time trace of absorption signal of MVKO at 319 K and 303 Torr (Table 4,6 Exp 1_f). The probe wavelength is (340±5) nm. The traces are vertically shifted for clarity. The time zero is set as the photolysis laser. The black solid curves are the fitting results of the model considering the kinetics of MVKO. The black dashed curves are the fitting results of the model considering the kinetics of (MVKO + U, the unknown species).

58

To check the relationship of MVKO and this slow decay signal, we added SO_2 as a scavenger of MVKO (See Figure 28). When MVKO is scavenged, we do not observe the slow decay any more, indicating that the slow decay signal is from a species related to MVKO, and this species is not correlated to the products of the reaction of MVKO with SO_2. We added this unknown species in our kinetic model (R1-7, Equations 12, 17-19), and the fitting results are shown in Figures 27, and 29, which well reproduce the time traces even for delay times up to 90 ms.
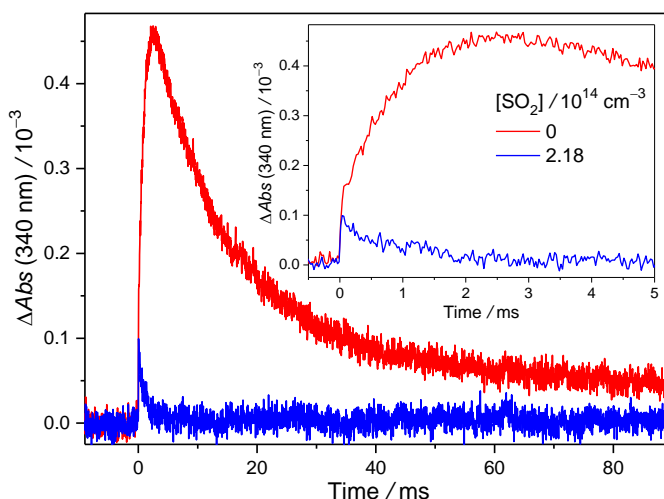
Figure 28. Time traces of the absorption signal of MVKO with $[SO_2] = 0/2.2 \times 10^{14}$ cm^{-3}. $P_{total} = 304$ Torr, $P_{O2} = 11$ Torr, $T = 300$ K, $Abs_{prec} = 0.033$, and laser fluence = 1.18 mJ cm^{-2}. The probe wavelength = (340±5) nm. The time zero is set as the photolysis laser. With $[SO_2] = 2.2 \times 10^{14}$ cm^{-3}, the absorption signal of MVKO is extinct after 5 ms delay time ($4\tau < 5$ ms). Inset plot shows the zoom in at short delay time.
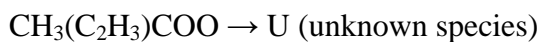
CH$_3$(C$_2$H$_3$)COO → Products + OH radical $\qquad$ (R5, $(1-\beta)k_{uni}$)

CH$_3$(C$_2$H$_3$)COO → U (unknown species) $\qquad$ (R6, βk_{uni})

U → Products $\qquad$ (R7, k_u)

$$[MVKO](t) = [MVKO]_0 e^{-k_{obs}t} + [adduct]_0 \frac{k_r}{k_r - k_{obs}}[e^{-k_{obs}t} - e^{-k_r t}]$$

$\qquad$ (Equation 12)

$$= [MVKO]_{total}\{\alpha e^{-k_{obs}t} + (1-\alpha)\frac{k_r}{k_r - k_{obs}}[e^{-k_{obs}t} - e^{-k_r t}]\}$$

$$\frac{d[U]}{dt} = \beta k_0 [MVKO] - k_u[U] \qquad \text{(Equation 17)}$$

$$[U](t) = [MVKO]_{total}\beta k_0 \frac{\exp(-k_u t)}{k_{obs} - k_r}\left\{\frac{\left[\exp((k_u - k_{obs})t)-1\right]\left[k_r - \alpha k_{obs}\right]}{k_{obs} - k_u} - \frac{k_r(1-\alpha)\left[\exp((k_u - k_r)t)-1\right]}{k_r - k_u}\right\}$$

$\qquad$ (Equation 18)

$$\Delta Abs = \sigma L[MVKO](t) + \sigma_u L[U](t) + C_0 \qquad \text{(Equation 19)}$$

where β represents the yield of U from the reaction of MVKO, k_u indicates the decay

rate coefficient of U, σ_u is the cross section of U at our probe wavelength. The meanings

of other symbols are the same as they are in Chapter 3.2.
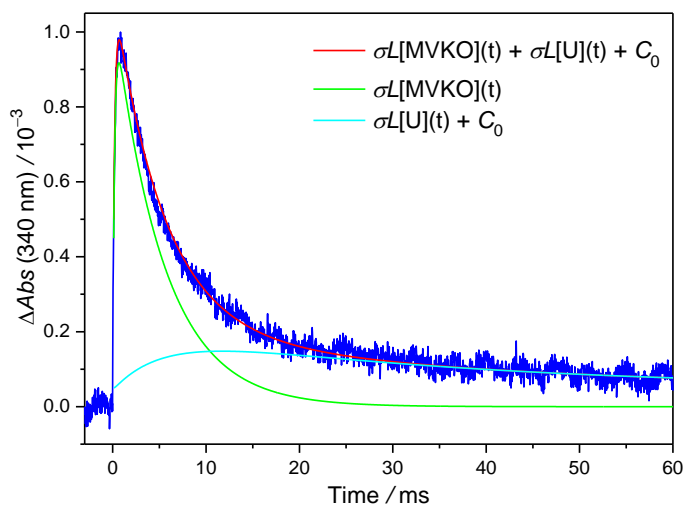
Figure 29. The time trace of the absorption signal of MVKO and its fitting result. (Table 5 Exp 1_f, $[SO_2] = 0$ cm^{-3}) The probe wavelength is (340 ± 5) nm. The time zero is set as the photolysis laser fired. The green curve is the fitting result of MVKO, and the cyan curve shows the fitting of the unknown species. The red curve is the sum of them.

The result of the unimolecular decomposition of MVKO with the fit model considering the unknown species U is shown in Figures 30-32 and Table 6. k_{uni} and k_{SO2} obtained from the model considering U are similar to those from the model without considering it. The effective yield of the unknown species, $\phi_{eff} = \sigma_u\beta/\sigma$, seems to be larger at a higher temperature.

61
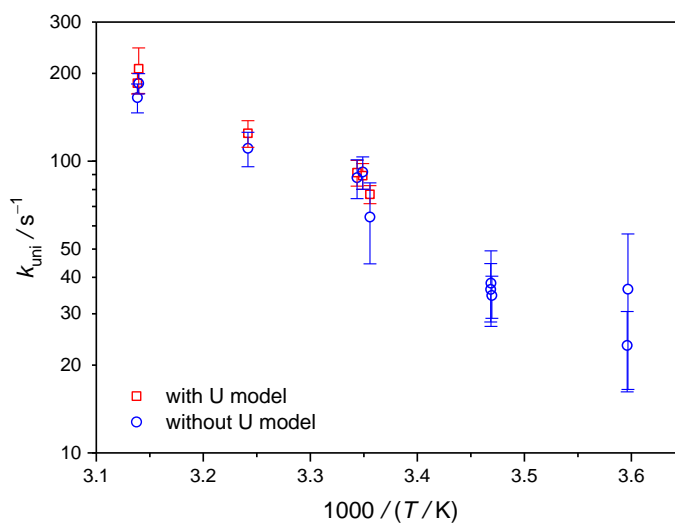
Figure 30. The Arrhenius plot of the unimolecular decomposition rate coefficient of

MVKO at 302 Torr. The y-axis is $\log_{10}$ scale. The red squares / blue circles represent the

results from the fit model with / without the unknown species.
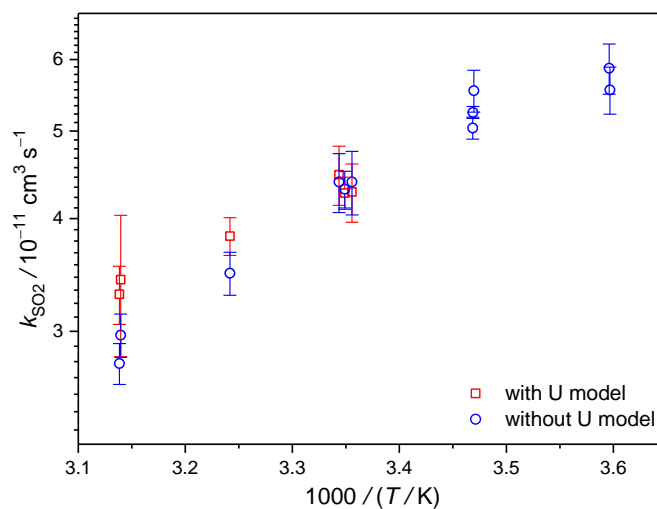
Figure 31. The Arrhenius plot of the reaction rate coefficient of MVKO with SO_2 at 302

Torr. The y-axis is $\log_{10}$ scale. The red squares / blue circles represent the results from

the fit model with / without the unknown species.

62
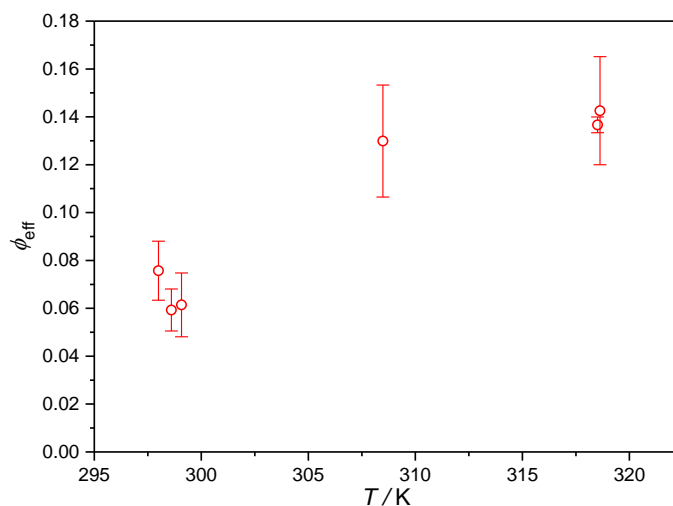
Figure 32. Plot of the effective yield of the unknown species ($\phi_{\text{eff}} = \sigma_u\beta/\sigma$) against

temperature.

Table 6. Summary of experiment conditions and fitting results of the unimolecular

decomposition of MVKO with the model considering the unknown species at 302 Torr

and 298-319 K. The probe wavelength is (340±5) nm. The fitting time range is 0.1−89.9

ms.

Exp #	$P_{\text{total}}{}^a$ / Torr	T / K	I^b / mJ cm^{-2}	$\sigma L[\text{MVKO}]_{\text{total}}$ / 10^{-3}	$1-\alpha$	k_r / s^{-1}	k_{SO2} /10^{-11} cm^3 s^{-1}	k_0 / s^{-1}	ϕ_{eff}	k_u / s^{-1}
1_a	302.2	318.7	1.06	1.09	1.00	5339	3.0	208	0.12	33
1_b	302.9	318.7	1.04	1.86	1.00	5590	3.5	208	0.12	27
1_c	302.8	318.7	1.05	1.48	1.00	5308	3.4	196	0.13	27
1_d	302.3	318.6	1.05	0.30	1.00	4954	3.4	197	0.18	50
1_e	302.4	318.6	1.03	0.65	1.00	5045	3.3	187	0.15	39
1_f	302.6	318.6	1.03	1.04	1.00	5102	3.1	191	0.13	30

1_g	302.2	318.6	1.06	0.32	1.00	4599	3.8	200	0.19	59
1_h	302.4	318.6	1.05	0.65	1.00	4954	3.0	193	0.13	38
1_i	302.9	318.6	1.04	1.47	1.00	5212	3.3	193	0.13	27
1_j	303.1	318.6	1.08	1.96	1.00	5453	3.3	198	0.13	27
2_a	301.9	318.5	3.18	1.71	1.00	5344	3.6	199	0.14	24
2_b	301.9	318.5	3.18	1.25	1.00	5175	3.3	195	0.13	25
2_c	301.7	318.5	3.17	0.75	0.96	4550	4.1	191	0.14	30
2_d	301.6	318.5	3.16	0.51	0.96	4337	2.6	222	0.13	39
3_a	303.5	308.5	1.05	1.99	0.96	2935	3.9	170	0.10	23
3_b	303.6	308.5	1.06	1.43	0.96	2773	3.8	158	0.11	23
3_c	303.5	308.5	1.07	0.85	0.96	2503	3.8	147	0.12	25
3_d	303.6	308.5	1.06	0.56	0.94	2359	4.0	138	0.15	43
3_e	303.7	308.5	1.07	0.31	0.93	2189	3.9	141	0.16	49
3_f	304.0	308.5	1.06	0.57	0.93	2381	3.6	134	0.13	41
3_g	303.9	308.5	1.06	0.32	0.94	2133	3.9	144	0.17	47
3_h	304.3	308.5	1.05	0.86	0.96	2443	3.4	144	0.12	32
3_i	304.5	308.4	1.05	1.27	0.95	2558	3.9	142	0.12	24
3_j	304.8	308.4	1.04	1.85	0.96	2747	4.0	154	0.11	24
4_a	301.2	298.0	1.04	1.66	0.90	1545	4.4	117	0.07	16
4_b	301.1	298.0	1.05	1.27	0.89	1310	4.2	109	0.07	20
4_c	301.0	298.0	1.05	0.76	0.88	1170	3.9	97	0.07	23
4_d	301.6	298.0	1.03	0.53	0.90	1158	3.9	96	0.06	28
4_e	301.6	298.0	1.03	0.32	0.87	998	4.8	90	0.09	58
4_f	302.3	298.0	1.01	1.75	0.88	1378	4.4	114	0.09	16
5_a	299.6	298.6	1.04	0.32	0.88	1081	4.5	106	0.06	38
5_b	299.7	298.6	1.03	0.54	0.89	1150	4.3	100	0.04	30
5_c	300.1	298.6	1.06	1.30	0.91	1469	4.2	109	0.06	17
5_d	299.6	298.6	1.06	0.57	0.87	1139	4.2	100	0.06	26
5_e	299.6	298.6	1.05	0.78	0.90	1273	4.1	99	0.06	20
5_f	299.8	298.6	1.05	1.29	0.91	1435	4.1	104	0.07	16
5_g	300.1	298.6	1.04	1.77	0.91	1539	4.5	114	0.06	16
6_a	300.0	298.9	3.17	1.54	0.90	1540	4.9	124	0.05	11
6_b	300.1	298.9	3.15	1.06	0.90	1398	4.4	114	0.06	17
6_c	300.2	299.0	3.14	0.60	0.90	1189	4.4	104	0.04	16
6_d	300.2	299.1	3.20	0.39	0.87	1066	4.2	99	0.08	31
6_e	300.3	299.1	3.18	0.24	0.85	934	4.4	110	0.08	36

6_f	300.5	299.1	3.17	0.39	0.87	1064	4.4	105	0.05	23
6_g	300.5	299.1	3.19	0.22	0.88	964	5.3	101	0.07	32
6_h	300.6	299.1	3.17	0.59	0.91	1226	4.1	104	0.05	34
6_i	300.8	299.2	3.15	1.59	0.90	1503	4.5	119	0.06	14
6_j	300.7	299.2	3.15	1.10	0.90	1393	4.4	106	0.08	16
6_k	300.7	299.1	3.14	1.59	0.91	1488	4.3	116	0.06	15

[a] Balanced by N_2.

[b] I represents laser fluence.

Table 7. Comparison of the two results with and without the unknown species U in the unimolecular decomposition of MVKO at 302 Torr. The probe wavelength is (340±5) nm. The fitting range is 0.1-89.9 ms.

Exp #	T / K	I^a / mJ cm^{-2}	without U model			with U model		
			k_{SO2} / 10^{-11} cm^3 s^{-1}	$(k_{uni} + k_{wall})$ / s^{-1}	k_{uni} / s^{-1}	k_{SO2} / 10^{-11} cm^3 s^{-1}	$(k_{uni} + k_{wall})$ / s^{-1}	k_{uni} / s^{-1}
1	318.6	1.05	2.8 ± 0.1^b	173 ± 6^c	165 ± 19^d	3.3 ± 0.2^b	193 ± 5^c	185 ± 15^d
2	318.5	3.17	3.0±0.2	193±7	185±15	3.4±0.6	215±18	208±37
3	308.5	1.06	3.5±0.2	119±5	111±15	3.8±0.2	132±4	125±13
4	298.0	1.04	4.4±0.4	72±8	64±20	4.3±0.3	85±2	77±6
5	298.6	1.05	4.3±0.2	100±4	92±12	4.3±0.2	97±3	89±9
6	299.1	3.17	4.4±0.3	96±4	88±13	4.5±0.3	99±3	91±9

[a] I represents laser fluence.

[b] The average ± 1 standard deviation of reaction rate coefficient of MVKO with SO_2 in an experimental subset.

[c] The error bar is the one standard deviation of $(k_{uni} + k_{wall})$.

[d] $\sigma_{k_{uni}}^2 = \sigma_{(k_{uni}+k_{wall})}^2 + \sigma_{k_{wall}}^2$.

4.5 Discussion

4.5.1 Unimolecular decomposition of Criegee intermediates

The kinetics of thermal unimolecular decompositions of Criegee intermediates has a structure dependence.[6] For small Criegee intermediates with hydrogen substitution group at the same side as the terminal oxygen, such as CH_2OO and *anti*-CH_3CHOO, the unimolecular decompositions are estimated to go through the formation of dioxirane, and the rate coefficients have been reported to be slow ($CH_2OO = (0.19\pm0.07)$ s^{-1}).[43, 45] For Criegee intermediates with a methyl group at the same side as the terminal oxygen, such as *syn*-CH_3CHOO and $(CH_3)_2COO$, the formation of vinyl hydroperoxide is estimated to be the main reaction pathway, and the tunneling of 1,4-H-migration plays an important role.[45] The thermal decay rate coefficients for *syn*-CH_3CHOO and $(CH_3)_2COO$ were reported to be $\sim10^2$ s^{-1}.[36, 38, 44, 46] However, in the case of *anti*-MVKO, which has a vinyl group at the same side as the terminal oxygen and is predicted to decompose via the formation of dioxole, a fast rate coefficient (2140 s^{-1} at room temperature) is predicted by theoretical calculations because of the low transition-state barrier.[4] As for *syn*-MVKO, similar to *syn*-CH_3CHOO and $(CH_3)_2COO$, the formation of vinyl hydroperoxide via 1,4-H-migration was estimated to be the most possible reaction pathway. The thermal decay rate coefficient was calculated to be 33 s^{-1} at room temperature,[4] which is of the same order of magnitude as our measured rate coefficient,

66

(71 ± 18) s^{-1} at 299 K and 100-503 Torr.

4.5.2 MVKO in the atmosphere

Possible removal pathways of MVKO include: (1) unimolecular decomposition. (2)

reaction with SO$_2$. (3) reaction with water vapor (4) reaction with HCOOH. For the

unimolecular decomposition of MVKO, we measured the rate coefficient to be (71 ± 18)

s^{-1} at 299 K and 100-503 Torr. The effective reaction rate coefficients of MVKO with

H$_2$O,(H$_2$O)$_2$, SO$_2$, and HCOOH are summarized in Table 8. We find that in the Amazon

region, where Criegee intermediates are estimated to be abundant, the effective

bimolecular rate coefficients are less than 20 s^{-1}. Thus, the unimolecular decomposition

is the predominant removal path of MVKO.

Table 8. Summary of the bimolecular rate coefficients of MVKO with atmospheric

species.

reactant	H$_2$O	(H$_2$O)$_2$	SO$_2$	HCOOH
k_{rxn} / cm^3 s^{-1}	10^{-18}-10^{-21} [,a]	10^{-14}-10^{-16} [,a]	4.0×10^{-11} [,b]	3.0×10^{-10} [,c]
[reactant] / cm^{-3}	2.3-7.7 x 10^{17} [,d]	0.1-1.2 x 10^{15} [,e]	0.01-1.4 x 10^{11} [f]	0.5-1.2 x 10^{10} [,g]
k_{rxn}[reactant] / s^{-1}	0.77-0.00023	0.01-12	0.04-5.6	1.5-3.6

[a] ref 5.
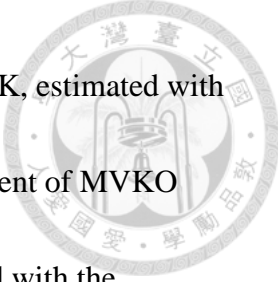
Caravan *et al.* has reported the modeled effect of the reaction of MVKO with SO$_2$ on global H$_2$SO$_4$ and the reaction of MVKO with HCOOH on global HCOOH with the global chemistry and transport model STOCHEM-CRI.[9] From their results, the concentration of H$_2$SO$_4$ would increase 10-20 % and that of HCOOH would decrease 15-20 % in the Amazon region after considering the reaction of MVKO with SO$_2$ and HCOOH.[9] The unimolecular decay rate coefficient of *syn*-MVKO used in their model is 33 s^{-1},[4] which is ~2 times slower than our result. Therefore, with our measured valve, (71±18) s^{-1}, the steady state concentration of MVKO would be ~2 times smaller than that from the estimation of Caravan *et al.* The increase in [H$_2$SO$_4$] would diminish to ~5-10 %, and the reduction of [HCOOH] would be only ~7.5-10 %. From our result, we can estimate that the gain of [H$_2$SO$_4$] resulted from the reaction of MVKO with SO$_2$ would be more at low temperature, due to the smaller unimolecular decay rate

coefficient of MVKO (k_{uni} would decrease ~39 % from 298 K to 288 K, estimated with the activation energy (8.3±2.5) kcal mol^{-1}) and the larger rate coefficient of MVKO with SO$_2$ (k_{SO2} would increase ~20 % from 298 K to 288 K, estimated with the activation energy (−3.1±0.8) kcal mol^{-1}).

4.5.3 Possible source for the unknown species

At this point, we do not know for sure the identity of the unknown species. From our experiments, we learn that the unknown species is a product from the unimolecular decomposition of MVKO, and its effective yield, ϕ_{eff}, could reach ~0.1 at ≥ 298 K. The possible candidates for the unknown species are (1) 2-hydroperoxidybuta-1,3-diene ((CH$_2$=CH)(CH$_2$)-COOH), a product from unimolecular decomposition of *syn*-MVKO through 1,4-H-migration (2) H$_2$C=C(O)-C(H)=CH$_2$, a conjugated system involving 5 electrons in 5 p-orbitals. It is a co-product of the OH channel. The absolute cross sections of these species have not been measured. The estimated absorption spectrum is shown in Figure 33. To clarify the unknown species, more study is needed.
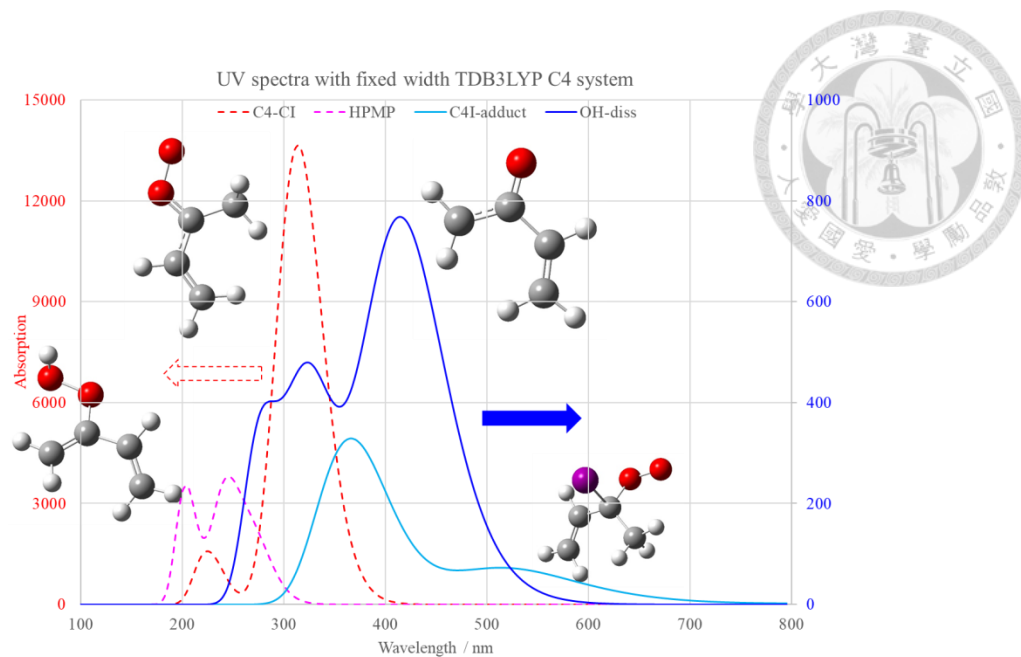
Figure 33. The estimated absorption spectra of $CH_3(C_2H_3)COO$ (dashed red line, left y-axis), $(CH_2=CH)(CH_2)-COOH$ (dashed magenta line, left y-axis), $H_2C=C(O)-C(H)=CH_2$ (solid blue line, right y-axis), and $CH_3(C_2H_3)CIOO$ (solid cyan line, right y-axis). (This plot is done by Dr. Kaito Takahashi.) The geometry optimization is done by B3LYP/6-311+G(2d,2p), and the vertically UV spectra are calculated by TD-B3LYP/aug-cc-pVTZ. The width of all peaks is fixed at 0.2 eV.

4.6 Conclusions

To measure the unimolecular decomposition rate coefficient of MVKO, we conducted the experiments at different initial concentrations of MVKO, and removed the effects of MVKO reactions of MVKO with radical byproducts and wall loss. The measured unimolecular decomposition rate coefficient is (71 ± 18) s^{-1} with an

insignificant pressure dependence at 299 K and 100-503 Torr. The activation energy was measured to be (8.3 ± 2.5) kcal mol^{-1} at 302 Torr and 278-319 K.
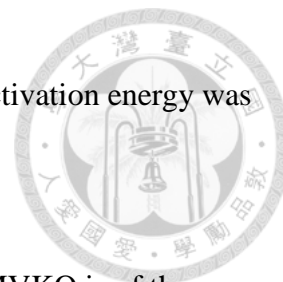
The measured unimolecular decomposition rate coefficient of MVKO is of the same order of magnitude as the previously estimated value, 33 s^{-1} at room temperature.[4] The unimolecular decomposition of syn-MVKO was predicted to go through 1,4-H-migration to form vinyl hydroperoxide, which is the same mechanism as those of Criegee intermediates with a methyl group at the same side as the terminal oxygen, such as syn-CH$_3$CHOO and (CH$_3$)$_2$COO. The thermal decay rate coefficients for syn-CH$_3$CHOO and (CH$_3$)$_2$COO have been reported to be $\sim10^2$ s^{-1}.[36, 38, 44, 46]

Considering the possible removal pathways of MVKO in the atmosphere, such as thermal decomposition and reactions with H$_2$O, SO$_2$, and HCOOH, the unimolecular decomposition would be the dominant removal pathway. This result could help the estimation of the influence of MVKO to the atmospheric chemistry be more accurate.

We observed a very slow decay signal at delay time longer than 30 ms for the time traces of MVKO at $T = 319$ K. A species correlated to MVKO could be the cause of this slow decay signal, and the time traces could be reproduced by the model considering the kinetics of this unknown species. The unimolecular decomposition rate coefficient of MVKO obtained from the model considering the unknown species is similar to that from the model without considering the unknown species. The possible source of this
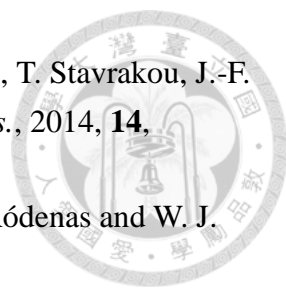
71

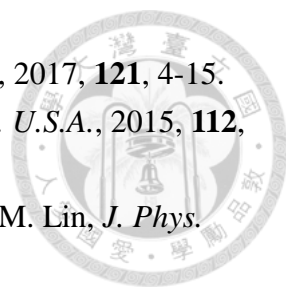unknown species is 2-hydroperoxidybuta-1,3-diene ((CH_2=CH)(CH_2)-COOH)) or

H_2C=C(O)-C(H)=CH_2, but more investigations are needed.

References

1. R. Criegee, *Angew. Chem. Int. Ed.*, 1975, **14**, 745-752.

2. L. Vereecken, *Science*, 2013, **340**, 154-155.

3. R. Atkinson, D. Baulch, R. Cox, J. Crowley, R. Hampson, R. Hynes, M. Jenkin, M. Rossi and J. Troe, *Atmos. Chem. Phys.*, 2006, **6**, 3625-4055.

4. V. P. Barber, S. Pandit, A. M. Green, N. Trongsiriwat, P. J. Wash, S. J. Klippenstein and M. I. Lester, *J. Am. Chem. Soc.*, 2018, **140**, 10866-10880.

5. L. Vereecken, A. Novelli and D. Taraborrelli, *Phys. Chem. Chem. Phys.*, 2017, **19**, 31599-31612.

6. J. J.-M. Lin and W. Chao, *Chem. Soc. Rev.*, 2017, **46**, 7483-7497.

7. Y.-P. Chang, H.-H. Chang and J. J.-M. Lin, *Phys. Chem. Chem. Phys.*, 2018, **20**, 97-102.

8. Z. C. J. Decker, K. Au, L. Vereecken and L. Sheps, *Phys. Chem. Chem. Phys.*, 2017, **19**, 8541-8551.

9. R. L. Caravan, M. F. Vansco, K. Au, M. A. H. Khan, Y.-L. Li, F. A. F. Winiberg, K. Zuraski, Y.-H. Lin, W. Chao, N. Trongsiriwat, P. J. Walsh, D. L. Osborn, C. J. Percival, J. J.-M. Lin, D. E. Shallcross, L. Sheps, S. J. Klippenstein, C. A. Taatjes and M. I. Lester, *Proc. Nati. Acad. Sci. U.S.A.*, 2020, **117**, 9733-9740.

10. J. D. Fenske, A. S. Hasson, A. W. Ho and S. E. Paulson, *J. Phys. Chem. A*, 2000, **104**, 9921-9932.

11. O. Welz, J. D. Savee, D. L. Osborn, S. S. Vasu, C. J. Percival, D. E. Shallcross and C. A. Taatjes, *Science*, 2012, **335**, 204-207.

12. G. T. Drozd, T. Kurten, N. M. Donahue and M. I. Lester, *J. Phys. Chem. A*, 2017, **121**, 6036-6045.

13. M. A. H. Khan, C. J. Percival, R. L. Caravan, C. A. Taatjes and D. E. Shallcross, *Environ. Sci.: Processes Impacts*, 2018, **20**, 437-453.

14. Y.-P. Lee, *J. Chem. Phys.*, 2015, **143**, 020901.

15. M. I. Lester and S. J. Klippenstein, *Acc. Chem. Res.*, 2018, **51**, 978-985.

16. D. L. Osborn and C. A. Taatjes, *Int. Rev. Phys. Chem.*, 2015, **34**, 309-360.

17. C. A. Taatjes, *Annu. Rev. Phys. Chem.*, 2017, **68**, 183-207.

18. T. A. Stephenson and M. I. Lester, *Int. Rev. Phys. Chem.*, 2020, **39**, 1-33.

19. K. Sindelarova, C. Granier, I. Bouarar, A. Guenther, S. Tilmes, T. Stavrakou, J.-F. Muller, U. Kuhn, P. Stefani and W. Knorr, *Atmos. Chem. Phys.*, 2014, **14**, 9317-9341.

20. M. J. Newland, A. R. Rickard, L. Vereecken, A. Muñoz, M. Ródenas and W. J. Bloss, *Atmos. Chem. Phys.*, 2015, **15**, 9521-9536.

21. M. Sipilä, T. Jokinen, T. Berndt, S. Richters, R. Makkonen, N. Donahue, R. Mauldin Iii, T. Kurtén, P. Paasonen and N. Sarnela, *Atmos. Chem. Phys.*, 2014, **14**, 12143-12153.

22. M. F. Vansco, B. Marchetti and M. I. Lester, *J. Chem. Phys.*, 2018, **149**, 244309.

23. Y.-P. Chang, C.-H. Chang, K. Takahashi and J. J.-M. Lin, *Chem. Phys. Lett.*, 2016, **653**, 155-160.

24. M. C. Smith, W.-L. Ting, C.-H. Chang, K. Takahashi, K. A. Boering and J. J.-M. Lin, *J. Chem. Phys.*, 2014, **141**, 074302.

25. W.-L. Ting, Y.-H. Chen, W. Chao, M. C. Smith and J. J.-M. Lin, *Phys. Chem. Chem. Phys.*, 2014, **16**, 10438-10443.

26. L.-C. Lin, W. Chao, C.-H. Chang, K. Takahashi and J. J.-M. Lin, *Phys. Chem. Chem. Phys.*, 2016, **18**, 28189-28197.

27. C. Yin and K. Takahashi, *Phys. Chem. Chem. Phys.*, 2018, **20**, 16247-16255.

28. W. Chao, J.-T. Hsieh, C.-H. Chang and J. J.-M. Lin, *Science*, 2015, **347**, 751.

29. J. A. S.P. Sander, J. R. Barker, J. B. Burkholder, R. R. Friedl, D. M. Golden, R. E. Huie, C. E. Kolb, M. J. Kurylo, G. K. Moortgat, V. L. Orkin and P. H. Wine, *JPL Publication*, 2011, **10-6**.

30. S. L. Manatt and A. L. Lane, *J. Quant. Spectrosc. Radiat. Transfer*, 1993, **50**, 267-276.

31. Y.-H. Huang, L.-W. Chen and Y.-P. Lee, *J. Phys. Chem. Lett.*, 2015, **6**, 4610-4615.

32. W.-L. Ting, C.-H. Chang, Y.-F. Lee, H. Matsui, Y.-P. Lee and J. J.-M. Lin, *J. Chem. Phys.*, 2014, **141**, 104308.

33. Y.-H. Lin, Y.-L. Li, W. Chao, K. Takahashi and J. J.-M. Lin, *Phys. Chem. Chem. Phys.*, 2020, **22**, 13603-13612.

34. C. A. Taatjes, O. Welz, A. J. Eskola, J. D. Savee, A. M. Scheer, D. E. Shallcross, B. Rotavera, E. P. F. Lee, J. M. Dyke, D. K. W. Mok, D. L. Osborn and C. J. Percival, *Science*, 2013, **340**, 177-180.

35. L. Sheps, A. M. Scully and K. Au, *Phys. Chem. Chem. Phys.*, 2014, **16**, 26701-26706.

36. R. Chhantyal-Pun, O. Welz, J. D. Savee, A. J. Eskola, E. P. F. Lee, L. Blacker, H. R. Hill, M. Ashcroft, M. A. H. Khan, G. C. Lloyd-Jones, L. Evans, B. Rotavera, H. F. Huang, D. L. Osborn, D. K. W. Mok, J. M. Dyke, D. E. Shallcross, C. J.

Percival, A. J. Orr-Ewing and C. A. Taatjes, *J. Phys. Chem. A*, 2017, **121**, 4-15.

37. H.-L. Huang, W. Chao and J. J.-M. Lin, *Proc. Nati. Acad. Sci. U.S.A.*, 2015, **112**, 10857-10862.

38. M. C. Smith, W. Chao, K. Takahashi, K. A. Boering and J. J.-M. Lin, *J. Phys. Chem. A*, 2016, **120**, 4789-4798.

39. K. T. Kuwata, E. J. Guinn, M. R. Hermes, J. A. Fernandez, J. M. Mathison and K. Huang, *J. Phys. Chem. A*, 2015, **119**, 10316-10335.

40. L. Vereecken, H. Harder and A. Novelli, *Phys. Chem. Chem. Phys.*, 2012, **14**, 14682-14695.

41. A. Novelli, K. Hens, C. Tatum Ernest, M. Martinez, A. C. Nölscher, V. Sinha, P. Paasonen, T. Petäjä, M. Sipilä, T. Elste, C. Plass-Dülmer, G. J. Phillips, D. Kubistin, J. Williams, L. Vereecken, J. Lelieveld and H. Harder, *Atmos. Chem. Phys.*, 2017, **17**, 7807-7826.

42. R. Atkinson, D. L. Baulch, R. A. Cox, J. N. Crowley, R. F. Hampson, R. G. Hynes, M. E. Jenkin, M. J. Rossi and J. Troe, *Atmos. Chem. Phys.*, 2004, **4**, 1461-1738

43. T. Berndt, R. Kaethner, J. Voigtländer, F. Stratmann, M. Pfeifle, P. Reichle, M. Sipilä, M. Kulmala and M. Olzmann, *Phys. Chem. Chem. Phys.*, 2015, **17**, 19862-19873.

44. Y.-L. Li, M.-T. Kuo and J. J.-M. Lin, *Rsc Adv.*, 2020, **10**, 8518-8524.

45. C. Yin and K. Takahashi, *Phys. Chem. Chem. Phys.*, 2017, **19**, 12075-12084.

46. Y. Fang, V. P. Barber, S. J. Klippenstein, A. B. McCoy and M. I. Lester, *J. Chem. Phys.*, 2017, **146**, 134307.

47. B. Ruscic, *J. Phys. Chem. A*, 2013, **117**, 11940-11953.

48. S. L. Paralovo, C. G. G. Barbosa, I. P. S. Carneiro, P. Kurzlop, G. C. Borillo, M. F. C. Schiochet, A. F. L. Godoi, C. I. Yamamoto, R. A. F. de Souza, R. V. Andreoli, I. O. Ribeiro, A. O. Manzi, I. Kourtchev, J. O. V. Bustillos, S. T. Martin and R. H. M. Godoi, *Sci. Total Environ.*, 2019, **650**, 996-1006.

49. P. Khare, N. Kumar, K. M. Kumari and S. S. Srivastava, *Rev. Geophys.*, 1999, **37**, 227-248.

50. R. W. Talbot, M. O. Andreae, H. Berresheim, D. J. Jacob and K. M. Beecher, *J. Geophys. Res.: Atmos.*, 1990, **95**, 16799-16811.